

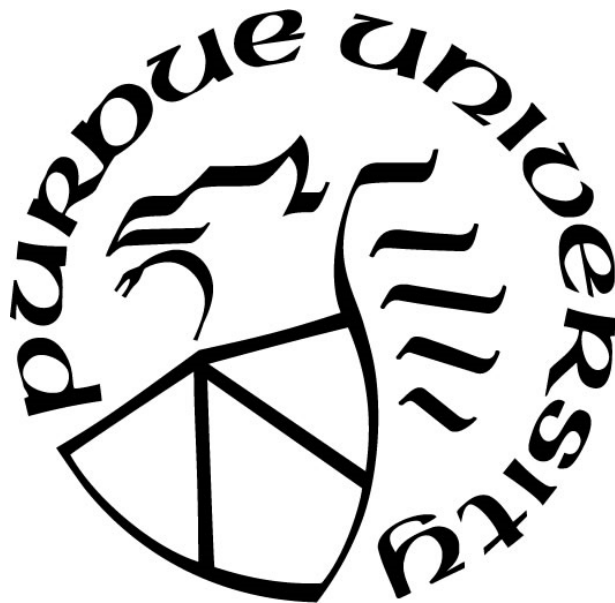
**WAVEFRONT MANIPULATION WITH METASURFACES  
BASED ON NEW MATERIALS**

by  
**Sajid Choudhury**

**A Dissertation**

*Submitted to the Faculty of Purdue University  
In Partial Fulfillment of the Requirements for the degree of*

**Doctor of Philosophy**



School of Electrical and Computer Engineering  
West Lafayette, Indiana  
August 2019

**THE PURDUE UNIVERSITY GRADUATE SCHOOL  
STATEMENT OF COMMITTEE APPROVAL**

Dr. Alexandra Boltasseva, Co-chair

School of Electrical and Computer Engineering

Dr. Alexander V. Kildishev, Co-chair

School of Electrical and Computer Engineering

Dr. Vladimir M. Shalaev

School of Electrical and Computer Engineering

Dr. Ali Shakouri

School of Electrical and Computer Engineering

Dr. Xiangfang Xu

School of Mechanical Engineering

**Approved by:**

Dr. D. Peroulis

Head of the Graduate Program

*Dedicated to my parents*

## ACKNOWLEDGMENTS

I sincerely acknowledge the help and guidance by my major advisor Prof. Alexandra Boltasseva. In stressful situations, she stood by my side as a mentor and helped me to overcome all difficulties and helped me to explore new opportunities and skills. I want to thank Prof. Alexander Kildishev for his enlightening advice. I extend my gratitude to Prof. Vladimir Shalaev, who would continuously encourage me to be more creative and pursue big dreams. I want to thank Prof. Ali Shakouri for his advice and support and thank Prof. Xiangfang Xu for agreeing to serve in my Ph.D. committee.

The gracious contribution of the people of my country to my education is perhaps understated. Even as a third world country, the taxpayer's money contributed to the free education that I received till Master's level and I gratefully acknowledge the support of my countrymen. My thirst for attacking new problems were instilled by the professors in my high-school and university, and I acknowledge their support and guidance that paved the way for my Ph.D. I particularly acknowledge Prof. Laila Noor Begum, Prof. Jaharlal Sarker, Prof. Anisul Haque, Prof. M. A. Matin, Prof. Mohammad Ali Chowdhury, Prof. Md Saifur Rahman for encouraging critical thinking and supporting me towards my admission.

I would like to gratefully acknowledge the support and help from all the current and former group members and colleagues from the Purdue Nanophotonics team for their constant support and guidance, namely Dr. Alexei Laguchev, Dr. Naresh Kumar Emani, Dr. Nataniel Kinsey, Dr. Justus Ndukaif, Dr. Zhaxylyk Kudyshev, Dr. Piotr Nyga, Dr. Alberto Naldini, Dr. Urcan Guler, Dr. Rohith Chandrashekar, Dr. Jingjing Liu, Dr. Jongbum Kim, Dr. Jeiran Fang, Dr. Zhuoxian Wang, Dr. Krishnakali Chaudhuri, Aveek Dutta, Dr. Clayton Devault, Di Wang, Soham Saha, Deesha Shah, Shaimaa Azzam, Harshavardhanareddy Eragamreddy, Samuel Peana, Sarah Chowdhury.

I would also express my gratitude to my parents, Prof. Naiyyum Choudhury and Prof. Shamima Choudhury, my sister, Dr. Sarah Choudhury, for always encouraging me and providing moral support.

## TABLE OF CONTENTS

LIST OF TABLES.....	8
LIST OF FIGURES .....	9
LIST OF SYMBOLS .....	11
LIST OF ABBREVIATIONS.....	12
ABSTRACT.....	14
1. INTRODUCTION.....	15
1.1 Introduction.....	15
1.2 Metasurface as a 2D metamaterial.....	15
1.3 Generalized Snell’s Law.....	16
1.4 Evolution of Metasurface.....	18
1.5 Pancharatnam Berry Phase Metasurface.....	20
2. MATERIAL PLATFORM FOR OPTICAL METASURFACE .....	21
2.1 Introduction.....	21
2.2 Plasmonic Metasurfaces.....	21
2.3 Dielectric Metasurfaces .....	24
2.4 Emerging Material Platforms for Optical Metasurfaces.....	26
2.4.1 Refractory Plasmonic Materials .....	26
2.4.2 Epitaxial Noble Metals .....	26
2.4.3 Silicon and its oxides and Nitrides .....	27
2.4.4 Titania .....	27
2.4.5 Transparent Conducting Oxides .....	28
2.4.6 Graphene and 2D materials .....	28
2.4.7 Phase Change Materials.....	29
2.5 Summary and Outlook .....	29
3. COLOR HOLOGRAM WITH EPITAXIAL SILVER BASED METASURFACE.....	30
3.1 Introduction.....	30
3.2 Hologram Generation.....	30
3.3 Numerical Simulation of Hologram Phase .....	32

3.4	Unit-cell design for metasurface hologram.....	33
3.5	Material Characterization.....	34
3.6	RGB Component Colors with Metasurface .....	36
3.7	Summary .....	39
4.	IMAGING PLASMONIC HEATING OF METASURFACE .....	40
4.1	Introduction.....	40
4.2	Theory of Time Domain Thermo-reflectance.....	40
4.3	Methods.....	41
4.3.1	Measurement Technique.....	41
4.3.2	Sample Preparation.....	42
4.3.3	Thermoreflectance of Survey of samples .....	43
4.4	Results.....	44
4.5	Arbitrary Temperature Profile Mapping.....	46
4.6	Summary.....	46
5.	REFRACTORY PLASMONIC METASURFACE FABRICATION FOR THERMO- PHOTOVOLTAIC APPLICATION .....	47
5.1	Introduction.....	47
5.1.1	Thermophotovoltaics (TPV):.....	48
5.1.2	Solar thermophotovoltaics (STPV): .....	48
5.2	Current and Future Challenges to incorporate TPV .....	48
5.3	Material Platforms for TPV .....	49
5.3.1	Conventional Refractory Materials.....	49
5.3.2	Refractory transition metal nitrides .....	49
5.3.3	Passivating refractory layers.....	50
5.4	Fabrication process for TiN based TPV emitter .....	51
5.4.1	Design Process.....	51
5.4.2	Prototype Fabrication.....	53
5.4.3	Prototype Characterization .....	54
5.4.4	Large area prototype fabrication.....	57
5.5	Concluding Remarks and Roadmap.....	58

6. CONCLUSION..... 59

REFERENCES ..... 60

VITA..... 80

PUBLICATIONS..... 81

## LIST OF TABLES

Table 2.1 Different Material Platforms with their Applications and Relative Advantages.....	25
---	----

## LIST OF FIGURES

Figure 1.1 Concept of metasurface as compact metamaterial .....	15
Figure 1.2 Intuitive interpretation of the generalized Snell's law .....	17
Figure 1.3 Evolution of different types of metasurfaces: plasmonic multiple-resonator [8], gap-plasmon resonators [9], Pancharatnam-Berry phase [10], blazed-binary grating [11], all dielectric metasurface[12], high contrast dielectric metasurfaces [12] .....	18
Figure 1.4 Polarization state C decomposed into A and B components and Poincaré sphere showing polarization states A, B, and C .....	20
Figure 2.1 Conventional and emerging material platforms for optical metasurfaces including noble and other commonly used in plasmonics metals; semimetals and intermetallic compounds exhibiting metallic behavior (such as metal nitrides, hydrides, oxides, borides, etc.); transparent conducting oxides; and dielectrics. ....	21
Figure 3.1 Simulated amplitude and phase profile of hologram (a)-(f) Amplitude and (g)-(l) Phase of the wavefronts from a letter P with dimension of 10 $\mu$ m. The total length of each axis of the images is 20 $\mu$ m (-10 $\mu$ m to 10 $\mu$ m shown in axis ticks). The image is assumed to be comprised of point sources, and the wavefront is calculated at distances away from the image plane. The distance of the wavefront (a),(g) 1 $\mu$ m, (b),(h) 3 $\mu$ m, (c),(i) 5 $\mu$ m, (d),(j) 7 $\mu$ m, (e),(k) 9 $\mu$ m and (f),(l) 10 $\mu$ m. ....	31
Figure 3.2 (a) 3D Illustration of a unit cell for a color. (b) Proposed supercell containing unit cells of each color. Blue, Green, and Red colored rectangle represent their respective slits with desired resonant frequency (c) s-polarized and (d) p-polarized transmission coefficient simulated for 3 different slit lengths, blue, green, and red represent three different lengths of slit. ....	32
Figure 3.3 Optical Properties and AFM image of the silver on MgO - (a) real and (b) imaginary part of permittivity of the silver film. (c) AFM measurement of surface roughness profile of the silver film. (d) TEM measurement of the silver film. Scale bars represent 5 nm.....	34
Figure 3.4(a) XRD counts of Epitaxial Silver film on MgO substrate. Inset shows the magnified silver peak (b) XRD counts of polycrystalline silver film.....	35
Figure 3.5 TEM image of (a)-(b) silver film with TiN wetting layer and (c)-(d) silver film with Germanium layer. Inset of (b) and (d) shows FFT .....	36
Figure 3.6 (a) Input image for the fabricated metasurface. (b)-(g)SEM Images of the fabricated metasurface structures. (b)-(d) scale bar 2.5 $\mu$ m, (e)-(g) scale bar 500 nm. (b)-(e) shows antennas for red color, (c),(f) shows antennas for green color and (d),(g) shows antennas for blue color. ....	37
Figure 3.7 (a) Experimental Setup (b-d) Final hologram image captured through CCD camera for (b) red, (c) green, and (d) blue hologram.....	38

Figure 3.8. Hologram observation by change of focus of the microscope. Left column shows the distance of the focal plane of the microscope set from the surface of the silver film. Each row corresponds to the focal plane for the hologram color .....	39
Figure 4.1 Experimental setup for Time Domain Thermo-reflectance.....	41
Figure 4.2 TiN nanodisk array sample preparation .....	42
Figure 4.3 Sample survey layout .....	44
Figure 4.4 Comparison between optical image and obtained thermal image.....	44
Figure 4.5 Temperature rise of patterned films: thermorefectance of (a) patterned (b) unpatterned film, (c) temperature change as a function of pump power and (d) thermorefectance image of unpatterned film.....	45
Figure 4.6 (a) Thermal map for the survey as measured, (b) simulated optical absorption of the array assuming periodic boundary condition, (c) fill factor of each array element. [176] (d) temperature change maxima shown for different array geometries, with simulated absorption and fill factor of each array.....	46
Figure 5.1 Thermophotovoltaics concept (a) Thermophotovoltaic configuration, using external heat source to generate radiative heating and (b) Solar Thermophotovoltaic configuration where solar irradiance is used for generating heat.....	47
Figure 5.2 TPV prototype schematic and modeling (a) schematic of TPV array showing different layers (b) cross-sectional view of a single unit cell .....	51
Figure 5.3 Fitted optical constants of TiN, SiN and simulated reflection (a) real part and (b) imaginary part of TiN permittivity for the 200nm and 30nm layers. (c) real part and (d) imaginary part of SiN permittivity (e) FDTD simulated reflection spectra of unit cell .....	52
Figure 5.4 Ebeam Prototype fabrication .....	54
Figure 5.5 SEM image of fabricated sample. Scalebar represents 1 $\mu$ m.....	55
Figure 5.6 Temperature dependent spectroscopic characterization of the TPV sample.....	56
Figure 5.7 Steps for nano-imprint lithography of emitter structures .....	57

**LIST OF SYMBOLS**

$k$	wavevector
$k_0$	vacuum wavevector
$c$	velocity of light in vacuum
$\epsilon'$	real part of relative dielectric permittivity
$\epsilon''$	imaginary part of relative dielectric permittivity
$R$	reflectivity
$T$	temperature

## LIST OF ABBREVIATIONS

ALD	atomic layer deposition
CMOS	complementary metal-oxide semiconductor
EIT	electromagnetically induced transparency
Ga:ZnO	gallium-doped zinc oxide
GST	germanium-antimony-tellurium
HAMR	heat assisted magnetic recording
HBN	hexagonal boron nitride
HSQ	hydrogen silsesquioxane
ICP-RIE	inductively coupled plasma reactive ion etch
IMT	insulator metal transition
ITO	indium doped tin oxide
LP	linear polarizer
LSPR	localized surface plasmon resonance
ND	neutral density
OTI	optical thermoreflectance imaging
PCM	phase change material
PMMA	poly(methyl methacrylate)
PSHE	photonic spin Hall effect
PTM	phase transition material
PV	photovoltaic
SiO <sub>2</sub>	silica
SPP	surface plasmon polariton
TDTR	time domain thermoreflectance

TiN	titanium nitride
TMAH	tetramethylammonium hydroxide
TPV	thermo-photovoltaic
VO <sub>2</sub>	vanadium dioxide
XRD	X-ray diffraction
ZrN	zirconium nitride

## ABSTRACT

Author: Choudhury, Sajid, M. PhD

Institution: Purdue University

Degree Received: August 2019

Title: Wavefront Manipulation with Metasurfaces based on New Materials.

Committee Chair: Alexandra Boltasseva, Alexander Kildishev

Metasurfaces, introduced as a compact 2D alternative of metamaterials, have developed into a vast field in recent times for light manipulation at an ultra-compact scale. Metasurface applications have found a place in the literature for compact alternatives to lens, holograms, polarizers, color filters. Plasmonic metasurfaces consisting of noble metals such as gold and silver provide light confinement on an unprecedented scale. Gold and silver grown conventionally on transparent substrates are polycrystalline, and exhibit losses and limit performance of the device. Moreover, these materials have a lower damage threshold and melting point. To circumvent the lower melting point and damage thresholds, new materials, and material growing techniques need to be researched.

In the first part of this work, a metasurface for color holography with an epitaxially grown silver thin film on a transparent substrate is shown. The demonstrated metasurface has been the first ever epitaxial silver metasurface that operated in the transmission mode. This plasmonic hologram has also been the thinnest metasurface hologram operating in transmission mode at the time of its reporting. The holographic image of all three basic color components of red, green, and blue has been demonstrated in the transmission mode. The control of color has been achieved by resonant sub-wavelength slits and the phase can be manipulated through altering slit orientation. This amplitude and phase control pave the way to applications of ultra-compact polychromatic plasmonic metasurfaces for advanced light manipulation. In the second part, we explore temperature rise due to the optical absorption in plasmonic structures. Titanium Nitride based metasurfaces structures are fabricated, that work in harsh environmental conditions and high temperature. A time domain thermo reflectance technique for rapid measurement of temperature is explored. Finally, a practical design prototype for thermo-photovoltaic (TPV) emitters using plasmonic metasurfaces is fabricated and characterized.

# 1. INTRODUCTION

## 1.1 Introduction

Harnessing, controlling, and understanding light has been a long-standing pursuit of human civilization, dating back to ancient times. After years of exploration and discovery, we find ourselves now surrounded with optical technologies which have advanced our ability to transmit data across the world at the speed of light, operating autonomous vehicles, detect microscopic lifeforms to save lives. Optics has revolutionized the world—yet, after so much progress and discoveries, most of our modern optical devices still resemble and rely on large optical components such as lenses, mirrors, and prisms for steering light. With current trends to progressively miniaturize technology, it is now essential to look for alternative methods to control light at extremely small dimensions. This miniaturization requires compact and planar devices with new functionalities that can now be realized via novel approaches that utilize artificially engineered optical materials.

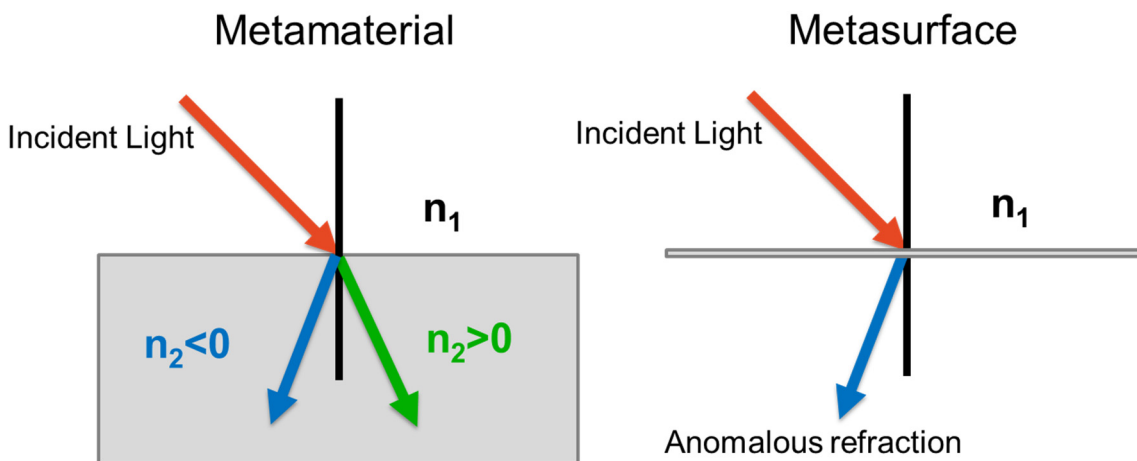


Figure 1.1 Concept of metasurface as a compact metamaterial

## 1.2 Metasurface as a 2D metamaterial

Artificially engineered materials can modify incoming optical waves in ways that are beyond naturally occurring bulk materials. The Greek word ‘meta’ means beyond, and the term ‘metamaterial’ is used to describe such class of materials. First proposed in the late sixties [1], composite materials with engineered optical properties regained excitement with the promise of

perfect lensing [2]. Metamaterials can exhibit negative effective permittivity or negative index, and thus can show refraction or reflection properties unattainable with naturally occurring materials. Such materials can realize effective negative refractive index [3], and thereby, can be utilized to make new devices such as lenses that can image beyond the diffraction limit [2] or invisibility cloaks [4]. Practical realization of such metamaterials is limited due to numerous challenges such as strict nano-fabrication requirements for layered structures, and significant optical losses in the dispersive optical materials.

The term ‘metasurface’ was first coined by Holloway *et al.* in 2005 as a surface equivalent of a metamaterial [5]. A metasurface or a metafilm can be described as a surface that can manipulate light like a metamaterial with reduced dimensionality. The concept is illustrated in Figure 1.1. The left side of the figure shows light incident at an oblique incidence at a material interface. If the index of the material,  $n_2$ , is positive, the light beam follows the green path. For a negative index,  $n_2 < 0$  the light beam will follow a different path satisfying Snell’s law and hypothetically, the blue arrow is shown in the figure as a possibility. For a metasurface, the surface itself can manipulate light propagation. As shown in the right panel of Figure 1.1, the surface can alter the path of the incident light and emulate refraction or even negative refraction.

### 1.3 Generalized Snell’s Law

A metasurface can redirect light in different directions through the application of abrupt phase shifts, which evolves into the generalized Snell’s law [6]. The generalized Snell’s law comes from the Fermat’s principle of least action, which states: “light travels between any two given points along the path of the shortest time” [7]. Here, simple trigonometry is used to derive the law. If we take the light ray in Figure 1.2 traveling from point A to point B, we can calculate the time  $t$  required for the light path by knowing the speed of light in each medium. Assuming both mediums are homogeneous with refractive index of  $n_1$  and  $n_2$  respectively, the time required for each path can be calculated as

$$t_1 = \frac{\sqrt{h_1^2 + x^2}}{c/n_1}, \quad t_2 = \frac{\sqrt{h_2^2 + (X - x)^2}}{c/n_2}$$

If the surface can introduce a position dependent abrupt phase change of  $\phi(x)$ , the time delay introduced by the phase is given by  $t_3 = \frac{\phi(x)}{2\pi f_0} = \frac{\phi(x)\lambda_0}{2\pi c}$ . Where  $\lambda_0$  and  $f_0$  are the wavelength and frequency of the incoming wave. The total time required for light to travel from point A to point B is given by  $t = t_1 + t_2 + t_3$ .

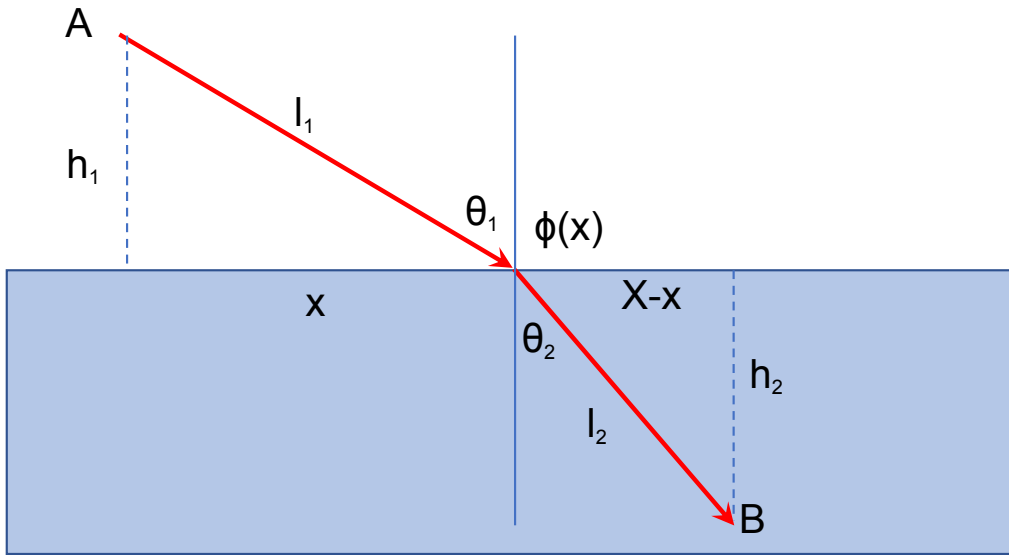


Figure 1.2 Intuitive interpretation of the generalized Snell's law

By taking derivative with respect to  $x$  we find,

$$\frac{dt}{dx} = \frac{x}{\sqrt{h_1^2 + x^2}} \frac{n_1}{c} + \frac{-(X-x)}{\sqrt{h_1^2 + (X-x)^2}} \frac{n_2}{c} + \frac{\lambda_0}{2\pi c} \frac{d\phi(x)}{dx}$$

We can find the path for the shortest time, by taking the derivative as zero. Also, angles  $\theta_1$  and  $\theta_2$  are given by  $\sin \theta_1 = x/l_1 = x/\sqrt{h_1^2 + x^2}$  and  $\sin \theta_2 = (X-x)/l_2 = (X-x)/\sqrt{h_1^2 + (X-x)^2}$ , we can get the generalized law of refraction as

$$n_1 \sin \theta_1 - n_2 \sin \theta_2 + \frac{\lambda_0}{2\pi} \frac{d\phi}{dx} = 0 \quad (0.1)$$

Therefore, if the phase can be modified abruptly by a surface, the laws of refraction would be dramatically different. Depending on the phase gradient,  $d\phi/dx$  the refracted light can even experience negative refraction as conceptualized in Figure 1.1.

#### 1.4 Evolution of Metasurface

A metasurface consists of a two-dimensional periodic arrangement of scattering elements. The scatterers are both smaller than the wavelength and separated by a sub-wavelength distance. The scattering elements can modulate both the amplitude and phase of incoming light, therefore enabling metasurfaces to control light at the sub-diffraction scale.

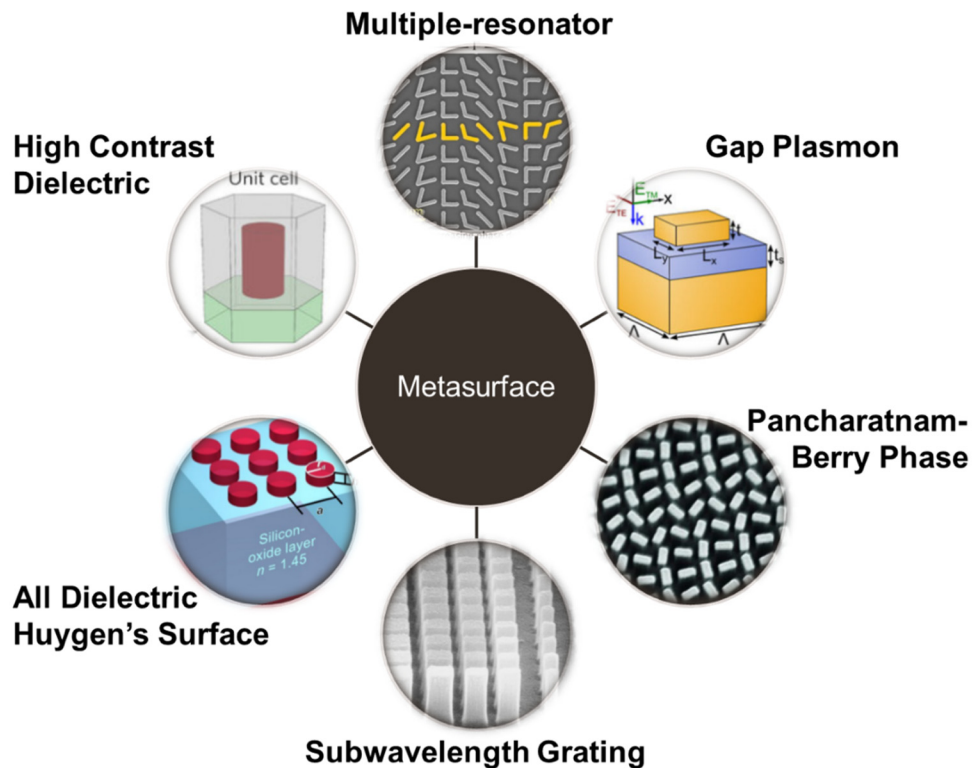


Figure 1.3 Evolution of different types of metasurfaces: plasmonic multiple-resonator [8], gap-plasmon resonators [9], Pancharatnam-Berry phase [10], blazed-binary grating [11], all dielectric metasurface[12], high contrast dielectric metasurfaces [12]

Localized surface plasmon resonance (LSPR) in metallic nanostructures arises from the free-electron oscillation coupling to incoming light. LSPR causes light confinement to structures many times smaller than the free-space wavelength of light. The first demonstration of metasurfaces

were done through resonator nanostructures of noble metals. By juxtaposing two rods at an angle to form a ‘V’ shape, the LSPR can be used to control phase. Researchers from Federico Capasso’s group first demonstrated anomalous reflection using resonant V-antennas and showed vortex beam generation at the infrared frequency [8]. Shalaev’s group at Purdue University demonstrated light bending at the visible spectrum with similar **multiple-resonator scheme** [13]. Although this scheme is beneficial for a conceptual demonstration of light manipulation, it suffers from low efficiency and lower cross-polarization conversion. Hybrid metasurfaces with a combination of nano-apertures and nanostructures showed improved efficiency [14]. Sergei Bozhevolnyi observed that by introducing a dielectric spacer layer between a metal back-reflector and metallic nanostructure array, a gap-plasmon mode can be engineered to have stronger confinement of light [9]. This **gap-plasmon metasurfaces** significantly improved the efficiency over multiple-resonator scheme — the presence of back-reflector limits the application of this kind of metasurfaces to only reflection-based applications. Single resonator structures of these metasurfaces provided a particular phase shift for a fixed frequency.

Geometric phase accumulation of circularly polarized light is shown to provide much finer control of phase. This accumulated phase, also called the **Pancharatnam Berry phase**, provided relatively broadband operation and simplified the design process of metasurfaces. All these types of plasmonic metasurfaces face the problem of losses inherent to the plasmon oscillations [15]. Low loss dielectric metasurface by utilizing graded index [11] or magnetic resonance [16][17] offer workaround losses of plasmonics. Reshaping wavefront with **subwavelength grating** emulating diffractive lens was proposed in the early 1990s as a method to prepare flat optical elements [11]. Decker *et al.* proposed arbitrary shaping of wavefront using Huygen’s principle, stating that each point at a waveform acts as a secondary source. As dielectric resonators can support both electric and magnetic mode through Mie scattering, they can be used as secondary sources. The scheme, coined as **all-dielectric Huygen’s metasurfaces**, showed full  $2\pi$  phase control with higher efficiency than plasmonic structures.

Further optical confinement was shown with **high-contrast dielectric** metasurfaces. First proposed by Faraon’s group, the dielectric resonators have a higher aspect ratio and support waveguide mode. The evolution of these different techniques for amplitude and phase manipulation is conceptually illustrated in Figure 1.3 and discussed in more details by Hsiao *et al.* [18].

### 1.5 Pancharatnam Berry Phase Metasurface

As mentioned in the earlier section, the geometric phase can enable phase control over a broad angular range. The geometric phase is termed as the Pancharatnam-Berry phase, after Shivaramakrishnan Pancharatnam, who first provided the concept for the generalized theory of interference between two coherent beams in different polarization [19] and Michael Berry, who independently identified it as phase accumulation in adiabatic quantum systems [20][21].

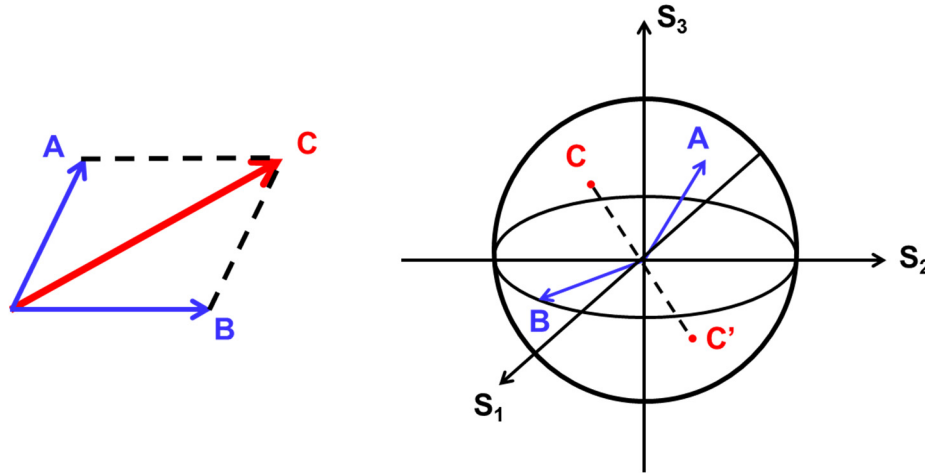


Figure 1.4 Polarization state C decomposed into A and B components and Poincaré sphere showing polarization states A, B, and C

An arbitrarily polarized beam, C can be decomposed into two components A and B. Figure 1.4 shows polarization states A, B, and C in a Poincaré sphere. Pancharatnam showed that the phase difference  $\delta$  between the beams is given by the solid angle formed by the C'BA triangle, where C' is the reciprocal point of C in the Poincaré sphere. Michel Berry showed that a similar phase accumulation occurs in adiabatic changes around a closed path in a quantum system. [22] Bomzon *et al.* from Erez Hasman's group first proposed to use Pancharatnam-Berry phase optical elements for converting wavefronts of cylindrical beams[23]. They were later used for metasurfaces by Kang *et al*[24], which led to additional applications involving the Pancharatnam-Berry phase, such as ultra-thin flat lenses[25], focusing mirrors[26], spin-dependent directional coupling[27], [28], spectroscopy[29], [30], polarization control[31], and ultra-compact tunable optical devices[32].

## 2. MATERIAL PLATFORM FOR OPTICAL METASURFACE

### 2.1 Introduction

Suitable material platforms are a necessity for getting the functionalities of phase manipulation at a subwavelength scale. Noble metals, as well as alternative materials, have been proposed for metasurface construction. Different applications of metasurfaces are enabled with new material discovery and fabrication breakthroughs. In this chapter, an overview of different material platforms for metasurfaces is given. Some of the content is reused with permission from [33] There are numerous review articles related to the development and seminal works of metasurfaces as well as applications and metasurfaces for specific material platforms [6], [18], [41], [42], [32], [34]–[40].

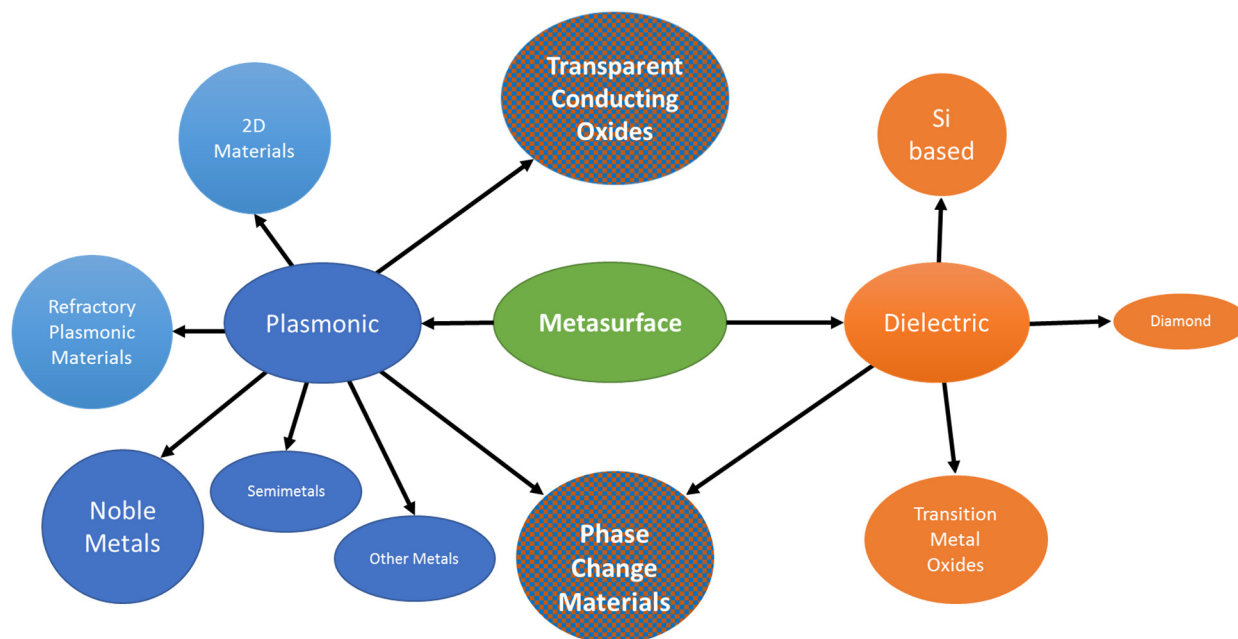


Figure 2.1 Conventional and emerging material platforms for optical metasurfaces including noble and other commonly used in plasmonics metals; semimetals and intermetallic compounds exhibiting metallic behavior (such as metal nitrides, hydrides, oxides, borides, etc.); transparent conducting oxides; and dielectrics. Figure is reused with permission from [33]. Copyright Degruyer 2018.

### 2.2 Plasmonic Metasurfaces

Tiny nanoparticles of noble metals are used to colorize glass since ancient times [43]. 4<sup>th</sup> Century Roman Lycurgus cup shows different colors when the light is shone through it and when the light

is reflected off from it. Polychrome luster decorations from the Abbasid era [44], and Cassius purple and ruby glass from the Renaissance period [45] demonstrate colorful pottery by using the characteristic red color of spherical gold nanoparticles. Such coloration can be explained by the interaction between nanoparticles and light, which forms the fundamental principle of plasmonics and plasmonic metasurfaces. Plasmonics deals with the coupling between the electromagnetic field and the electronic oscillations of material. A plasmon is a quantum of free electron oscillation. Free electron clouds in a metal can couple to light at an interface between metal and dielectric media and create surface plasmons. With adequately designed nanostructures made from metals, the surface plasmons make it possible to control light at the sub-diffraction scale.

Not only the plasmonic nanostructures can guide light at the nanoscale, but they can also increase the local intensity of the electromagnetic field by orders of magnitude. This enhancement is possible due to the strong local field confinement near the metal surface of a nanostructure. For metallic subwavelength structures or nanoparticles, the electric field of incoming radiation can polarize the conduction electrons. The resulting plasmon oscillations are distributed over the nanoparticle volume and are localized within the particle. These plasmon oscillations are termed localized surface plasmons (LSPs). The displacement of the electron clouds from the lattice generates a restoring force that tries to pull the electrons back into the lattice. The nanoparticle, therefore, acts as an oscillator driven by the incoming field together with restoring Coulomb force and behaves as a simple dipole in the direction of the electric field. When the frequency matches the resonance-frequency defined by the shape of the particle, LSP resonance occurs, enhancing local field amplitude. The nanostructures can also introduce a local phase shift to the incoming light beam and manipulate its wavefront.

The concept of local phase shift generation using plasmonic nanostructures can be employed by introducing abrupt phase jumps with metasurfaces. When light travels through a plane that can introduce abrupt phase change, it has been shown that the light propagation needs to be explained with a modification of Snell's law by introducing an artificially engineered phase-gradient term. The resulting phase-gradient from a sub-wavelength thick structure is shown to bend light in anomalous directions [8]. Since most of the conventional optical devices rely on amplitude or phase modulation of the incoming light, the ability of plasmonic nanostructures to introduce the abrupt phase shift can be used to engineer ultra-compact optical devices. An early demonstration

of photonic spin Hall effect, with polarization dependent splitting of light, is also achieved by plasmonic metasurface [46]. Seminal work on plasmonic antennas with aluminum [47] spearheaded the field of Al-based plasmonic metasurfaces. Many of the first applications of metasurfaces demonstrate imaging and sensing at the nanoscale, namely sub-diffraction lensing [10], [25], [48]–[51], spectroscopy [52], monochromatic holography [53]–[60], color holography [61]–[64], polarization converters [23], [31], [65]–[68], vortex plates [69]–[71], invisibility cloaks [72], polarization-selective elements [30], [73]–[75], etc.

Despite all the promising applications of plasmonic metasurfaces, optical losses in plasmonic devices severely limit their use in replacing conventional optical elements. As electron clouds in the metal oscillate while interacting with the incoming electromagnetic wave, they experience scattering in the material that causes heat generation. Although for the best plasmonic material, low loss (small imaginary part of permittivity) and high plasmonic property (large negative real part of permittivity) are essential, the losses cannot be avoided entirely. Even for an ideal plasmonic material with negligible loss, nano-structuring the metal causes the magnetic field of an incoming electromagnetic wave to be truncated as the wave interacts with the free electrons of the structure. Truncating the magnetic field, in turn, results in the conversion of stored magnetic energy into kinetic energy of electrons and causes a loss termed the Landau damping [76]. Compared to dielectric metasurfaces discussed in the next section, plasmonic metasurfaces will be therefore inherently less efficient but will have tighter field confinement, broader bandwidth, and smaller device footprint. For applications specific to plasmonic metasurface, the tradeoff between field confinement and loss must be made. Plasmonic metasurfaces are particularly useful, however, when optical losses are desired, such as in heating or absorber devices. Scattering loss minimization for plasmonic metasurface has been proposed through impedance matching [77], but the rest of the losses are inherent in plasmonic systems. Applications for plasmonic metasurfaces are emerging exploiting their ability to strongly confine field such as color filter and displays [78]–[80], enhanced harmonic generation [81]–[83], improved nonlinearity [84], [85], detection sensitivity improvement [86]–[88], absorbers [89]–[91], perfect absorber and efficient thermal emitters [92]–[94], photocatalysis [95], high temperature applications such as thermophotovoltaics [96], heat-assisted magnetic recording [97] etc.

Conventional plasmonic materials such as gold and silver have been historically used for most of the early metasurface applications. Bulk silver has excellent plasmonic properties in the visible frequencies but evaporated silver, which is most commonly used in metasurfaces due to the relatively easy fabrication, is prone to be lossier due to electron scattering at grain boundaries. Also, it is fundamentally challenging to grow ultrathin (on the order of few nanometers) gold and silver films, because these two materials tend to form nano-islands rather than continuous films at thicknesses below 10 nm. From the fabrication standpoint, gold and silver are also not compatible with the standard complementary metal-oxide-semiconductor (CMOS) technology, as silver has low chemical stability and gold is quickly diffused into the substrate. Additionally, these noble metals have low melting temperatures. Therefore, the nanostructures made of noble metals easily deform at elevated temperatures.

Consequently, noble metals are not suitable for high-temperature applications, which is a dilemma for plasmonics because the plasmon oscillations unavoidably heat the metals significantly, at least within the spatial field confinement. For stronger field confinement and high-temperature applications beyond noble metals' capabilities, new plasmonic materials are necessary. Study of alternative plasmonic materials has become a new field of itself and has found functional devices using the merger of metasurface with these materials' applications [98].

### **2.3 Dielectric Metasurfaces**

All-dielectric metasurfaces have been developed as a possible answer to the inherent optical losses associated with plasmonic metasurfaces. Dielectric metasurfaces are based on the collective light scattering (known as Mie scattering) off the constituent high-index dielectric nanoparticles with dimensions comparable to the wavelength of light inside the particles [99]–[102]. Because of the low-loss feature, all-dielectric metasurfaces significantly surpass plasmonic metasurfaces in efficiency and resonance quality factor.

Table 2.1 Different Material Platforms with their Applications and Relative Advantages

Classification	Examples	Wavelength range	Advantages	Limitations	Applications
Noble metal	Au, Ag, Al, Cu...	Visible-Mid IR	Established fabrication; Plasmonic in the UV part of spectrum (Ag, Al); Small device footprint; High field concentration	Low melting point; Lack of tunability	Proof of concept demonstrations
Refractory	TiN, ZrN, HfN, W...	Visible-Mid IR	High durability; High melting point; CMOS compatible	Strict fabrication requirements	High temperature and high intensities
2D	Graphene, MXene, phosphorene, MoS <sub>2</sub> , WSe <sub>2</sub> , WS <sub>2</sub> ...	Near-Mid IR	Dynamic tunability (electrical); Fast modulation; Large field confinement; Compactness/lightweight; Mechanical flexibility; Lower loss than noble metals in Near IR	Weak optical response	Dynamically tunable and flexible devices
Phase change	GST, VO <sub>2</sub> , YH <sub>2</sub> , MgH <sub>2</sub> , PdH <sub>2</sub> , SmNiO <sub>3</sub>	Near-Mid IR	Dynamic tunability (temperature); Large optical modulation	Slow modulation	Non-volatile reversible optical switches
Transparent conducting oxides	ITO, Ga:ZnO, Al:ZnO	Near-Mid IR	ENZ in Near IR; Ultrafast tunability (optical, electrical, temperature)	Low field confinement	Ultra-fast optical modulators
Dielectric	Si, TiO <sub>2</sub> , SiO <sub>2</sub> , Si <sub>3</sub> N <sub>4</sub> , diamond	Visible-Near IR	Near zero optical loss; Mechanical and chemical robustness	Larger device footprint; Low field confinement	Highly efficient metasurfaces

Electromagnetically induced transparency (EIT) with a quality factor of  $\sim 600$  has been demonstrated in all-dielectric metasurfaces [103], [104], whereas similar type of plasmonic EIT metasurfaces have a quality factor on the order of 10.

Dielectric nanostructures support both electric and magnetic resonances that paves way to functionalities that were previously not possible with plasmonic metasurfaces. Dielectric resonators can support both electric and magnetic resonance. If the two resonances are excited in phase and equal strength, backscattering can be minimized due to destructive interference [99], [105].

## **2.4 Emerging Material Platforms for Optical Metasurfaces**

### **2.4.1 Refractory Plasmonic Materials**

As mentioned earlier, noble metals are incompatible with CMOS process and have a lower melting point and less stable at higher temperature. Refractory materials such as titanium nitride (TiN), zirconium nitride (ZrN), tungsten (W) have been demonstrated to have plasmonic properties. Visually, TiN is very similar to gold and has been used on the domes of Churches as an alternative to gold, which suggests they have similar optical properties. TiN based broadband metasurfaces absorber was demonstrated with 87% absorption in the 400-600nm spectral window [106]. The authors demonstrated that the structures survived higher incident intensity and temperature, where similar gold nanostructures were damaged. For local heating application, the array of disk-shaped TiN nanoparticles outperform Au based similarly structured arrays [107]. ZrN based metasurfaces was demonstrated to have photonic spin Hall effect (PSHE) with 60% efficiency [108].

### **2.4.2 Epitaxial Noble Metals**

Among noble metals, silver has the highest negative permittivity in the visible frequency regime. For application in plasmonic metasurfaces where high efficiency is desired, epitaxially grown noble metals can outperform noble metals grown with standard evaporation techniques. Epitaxial silver film can be deposited with lattice matching [109][110][111], aluminum doping [112], stabilization layer [113]. In their letter, Liu *et al.* showed that a metasurface, when engineered adequately with periodic gratings, can give rise to flat or hyperbolic iso-frequency dispersion contours. The so-called “hyperbolic metasurface” was first demonstrated through epitaxial silver

by High *et al.* [114]. Their fabricated metasurface showed in 2D some of the critical characteristics of bulk hyperbolic metamaterials, such as negative refraction and diffraction-free propagation. Though silver itself is a conventional plasmonic material, epitaxial silver, having optical properties of bulk silver at nanoscale thicknesses, opens new dimensions for plasmonic metasurface design at visible wavelengths with strong field confinement and lower loss.

### 2.4.3 Silicon and its oxides and Nitrides

As mentioned before, dielectric metasurfaces have a clear advantage over their plasmonic counterparts in low-loss applications. Silicon and its native oxide and nitrides have the advantage of being able to use the existing CMOS processing lines for device fabrication. Silicon is lossy in the visible frequency spectrum, and most of its applications are in the near-infrared region. For a great review on different Si-based metasurfaces, Staude and Schilling's review can be referred to [100]. Combination of electric and magnetic resonance was proposed by Decker *et al.* to produce near unity transmission with phase dependence on the wavelength of incident light [16]. Silicon-based metasurfaces has been shown for various on plane optical applications such as vortex beam generation [75][115], EIT [104], refractive index sensing [116], planar focusing lens [117][118][119], polarization converter [12], electromagnetic mode conversion [120][121], color filtering [122]. Both silica ( $\text{SiO}_2$ ) and silicon nitride ( $\text{Si}_3\text{N}_4$ ) are transparent in the visible and have significantly lower optical losses.  $\text{Si}_3\text{N}_4$  can give higher index contrast compared to  $\text{SiO}_2$ . High focusing efficiency metasurfaces with  $\text{Si}_3\text{N}_4$  is demonstrated in the literature [123].

### 2.4.4 Titania

Titania ( $\text{TiO}_2$ ) has a higher refractive index (2.4) than  $\text{SiO}_2$  or  $\text{Si}_3\text{O}_4$ , and zero optical losses in the visible. Titania is more commonly used for dielectric metasurfaces applications where high index contrast is essential. First known to date effort to apply titania in planar optical lenses was done by Lalanne *et al.*, who demonstrated up to 89% efficiency in visible wavelength with refractive index modulation [11], [124], [125]. Federico Capasso group from Harvard University pioneered the field of phase gradient metasurfaces with titania, with highly uniform atomic layer deposited (ALD) deposited titania showing lenses with 86% efficiency at 405nm wavelength [10]. High numerical aperture lens [126], polarization insensitive lens [127], multiplexed hologram [128], high resolution chiral spectroscopy [129], chiral spectroscopy [130], vortex beam generation [131]

is demonstrated with titania based metasurface. Strain-dependent tunable metasurface [132] and color filtering [133] is also demonstrated with titania based metasurface.

#### 2.4.5 Transparent Conducting Oxides

Metal-oxides are shown to have great promise as alternative materials for plasmonic applications due to their large charge donor densities [134][135]–[138]. Gregory *et al.* showed indium doped tin oxide (ITO) based metasurfaces with split ring resonators. Kim *et al.* demonstrated gallium-doped zinc oxide (Ga:ZnO) based highly sensitive mid-infrared refractive index sensor [51] and near-infrared quarter waveplate metasurfaces [171]. As the Metal oxides are less plasmonic compared to noble metals, they are easily outperformed by gold or silver for static applications. However, the metal oxides show broad tunability of optical properties. Abb *et al.* showed that the optical response of gold nanoantennas can be modified at ultrafast time scale by optical pumping [139]. Ultrafast switching of optical properties. Robert Chang's group showed subpicosecond recombination rates with ITO nanorod structures [140]. ITO thin film based metasurfaces is demonstrated as effective gate tunable modulator with ~30% change in reflectance with 2.5V bias voltage and full  $\pi$  phase control [141].

#### 2.4.6 Graphene and 2D materials

As a monolayer of carbon atoms, graphene is exceptionally thin two-dimensional material. Recent development of nanofabrication processes enabled successful demonstration of graphene metasurfaces with nanoribbons [142][143][144], nanorings [145]. Getting the intrinsic graphene resonance to wavelengths of visible or near-IR remain a challenge, as it would require nanostructures smaller than 5nm and significantly higher doping level (~1eV). In addition to the intrinsic graphene plasmonic response, the tunable optical property of graphene is also explored for metasurfaces. Emani *et al.* demonstrated electrical tuning of Fano-type resonance with graphene at ~2.4  $\mu\text{m}$  wavelength with ionic gel top gating [146]. Based on the dynamic tuning of graphene, applications such as protein monolayer sensing [147], photodetection [87], [148]–[151], optical modulator [152][153]. In combination with hBN, graphene has been demonstrated to have higher optical confinement [154]. Huang *et al.* demonstrated multilayer graphene ribbons can have higher sensitivity than single layer devices, and demonstrated highest sensitivity for refractive index sensing [155].

### 2.4.7 Phase Transition and Phase Change Materials

Dynamic control of metasurfaces properties can be realized through phase transition materials (PTM) and phase change materials (PCM). Metal to insulator transition properties of these materials are well studied [156], and they are suitable candidates where dynamic tuning is desired. PTMs are naturally reversible and return to their original stage when input excitation is absent for a period of time. PCMs are non-volatile, meaning they would remain in their changed phase until another 'reset' excitation forces them back to the original stage. PTM Vanadium dioxide ( $\text{VO}_2$ ), and PCM germanium-antimony-tellurium (GST), both show promising applications.  $\text{VO}_2$  exhibits four orders of magnitude resistivity change when the temperature is changed beyond its undergoing insulator-metal-transition (IMT) temperature. Resonance frequency shift of up to 20% is demonstrated with split ring resonators on  $\text{VO}_2$  thin film [157] with temperature induced phase transition. All-optical switching [158] and gated switching [159] is also shown with  $\text{VO}_2$  based metasurfaces. GST as a PCM has more potential to have switchable dynamic control. Gholipour *et al.* showed resonance switching of gold nanoantennas by putting a ZnS/GST/ $\text{SiO}_2$  layer on top of the antennas. The GST sandwich layer could modulate the reflection spectra by 400% in near and mid-IR regions [160]. GST layers has been used to demonstrate dynamic switching of reflection in Mid IR of Al nanoantennas [161], mid-IR temperature-dependent switchable perfect absorber [162] and mid IR circular dichroism [163].

## 2.5 Summary and Outlook

In this chapter, conventional and emerging material platforms for metasurfaces devices and applications are reviewed. Two exceptionally suitable material candidates for static use are epitaxial silver when the lowest loss is desired and refractory materials when high-temperature applications are required. In the following sections, the device application for these two materials are demonstrated in detail.

### **3. COLOR HOLOGRAM WITH EPITAXIAL SILVER BASED METASURFACE**

#### **3.1 Introduction**

This chapter introduces monocrystalline silver grown on a transparent substrate as a material platform for plasmonic metasurfaces. It has been demonstrated previously that Silver (001) can be grown epitaxially on MgO (001) substrate with the help of epitaxial TiN layer[164]. Demonstrated silver films show the lowest loss for silver grown on a transparent substrate. Monochromatic holograms have been created at subwavelength scale using extreme light confinement of resonant plasmonic structures, such as V-antennas[53], nanorods[56], nano-pillars[165], subwavelength gratings[166]. Principally, the combination of the three basic element colors, red, green, and blue, can be utilized to make a color image. Most plasmonic metals are dielectric or less plasmonic in the blue region. It is therefore difficult to produce a blue color component for multicolor holograms using a plasmonic metasurface. Color holograms have been generated with white light excitation of surface plasmons in diffraction gratings[167], [168]. Orthogonal polarizations with different resonant structures have also been used to produce dual color holograms in reflection mode[59]. Recently, multicolor holograms have been demonstrated with metal-insulator-metal gap plasmonic structures[62], metallic slits[63] and rotated dielectric nanobars[169], [170]. The designed Pancharatnam-Berry phase manipulating metasurface can modify the phase of an incoming light to produce a color hologram at a virtual imaging plane. The paper also illustrates a scheme to create multicolor holograms in the visible range with all color components present. The demonstrated experimental scheme is achieved with the help of an ultra-smooth 50-nm thick silver film, that has best demonstrated optical property grown on a transparent substrate. The metasurface design scheme paves the way to developing ultra-compact polychromatic optical elements at visible wavelengths. The work has been published and the text and figures are reused with permission from [64] and copyrighted to Wiley .

#### **3.2 Hologram Generation**

A hologram can be generated by controlling the amplitude and phase of incoming light. According to Huygen's principle, every point in wavefront acts as a secondary source. So, if the amplitude

and phase of each point of a wavefront of an image are known, the image can be constructed by inverse design. This inverse designing can be done by placing a point source at each point of the wavefront with the same amplitude and phase as the initial incident wave. The electromagnetic field emitted from a point source can be obtained through the Green function representation [53],

$$G = -\frac{1}{4\pi|\mathbf{r}_d - \mathbf{r}_s|} \exp\left(i\frac{2\pi}{\lambda}|\mathbf{r}_d - \mathbf{r}_s|\right) \quad (3.1)$$

Where  $|\mathbf{r}_d - \mathbf{r}_s|$  gives the distance between a particular point in space and the source point. Hence, the amplitude and phase of the wavefront,  $A(\mathbf{r})\exp(i\Phi(\mathbf{r}))$  at a distance away from the point sources can be calculated by summing over the complex intensities of the point sources.

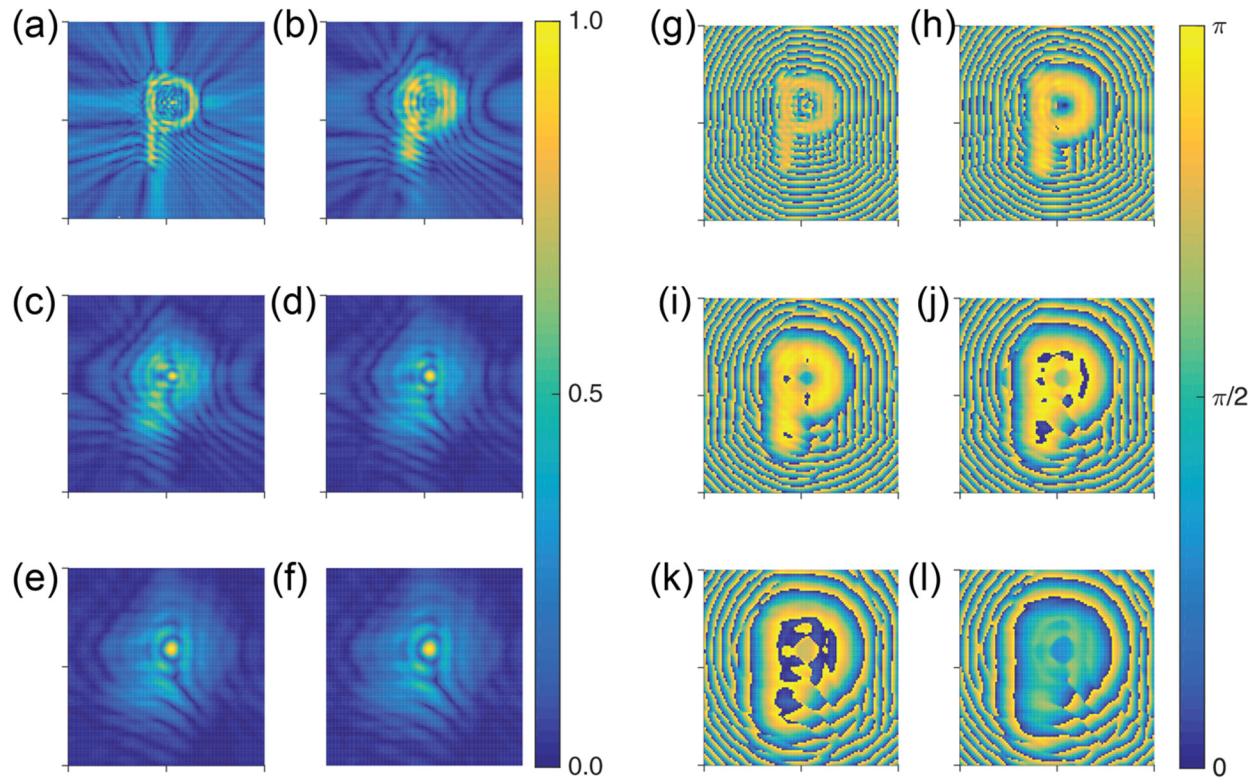


Figure 3.1 Simulated amplitude and phase profile of hologram (a)-(f) Amplitude and (g)-(l) Phase of the wavefronts from a letter P with dimension of  $10\mu\text{m}$ . The total length of each axis of the images is  $20\mu\text{m}$  ( $-10\mu\text{m}$  to  $10\mu\text{m}$  shown in axis ticks). The image is assumed to be comprised of point sources, and the wavefront is calculated at distances away from the image plane. The distance of the wavefront (a),(g)  $1\mu\text{m}$ , (b),(h)  $3\mu\text{m}$ , (c),(i)  $5\mu\text{m}$ , (d),(j)  $7\mu\text{m}$ , (e),(k)  $9\mu\text{m}$  and (f),(l)  $10\mu\text{m}$

If we take the inverse problem and assume point sources with amplitude  $A(\mathbf{r})$  and phase  $\Phi(\mathbf{r})$  placed at discrete points in space, we can reconstruct the original images. The amplitude and phase of each color components have to be calculated at the wavefront to create a color hologram. While restoring the image, quantization noise would be present due to a finite number of sources at the wavefront plane. This noise can be minimized by placing the sources as compact as possible.

### 3.3 Numerical Simulation of Hologram Phase

To illustrate the amplitude and phase profile of the wavefront, we consider an image of the letter **P** with length  $10\ \mu\text{m}$  and calculate the amplitude and phase points at various distances. Figure 3.1(a)-(f) show the amplitude profile and Figure 3.1(g)-(l) show the phase profiles at different distances from the image plane at  $\lambda = 676\ \text{nm}$ .

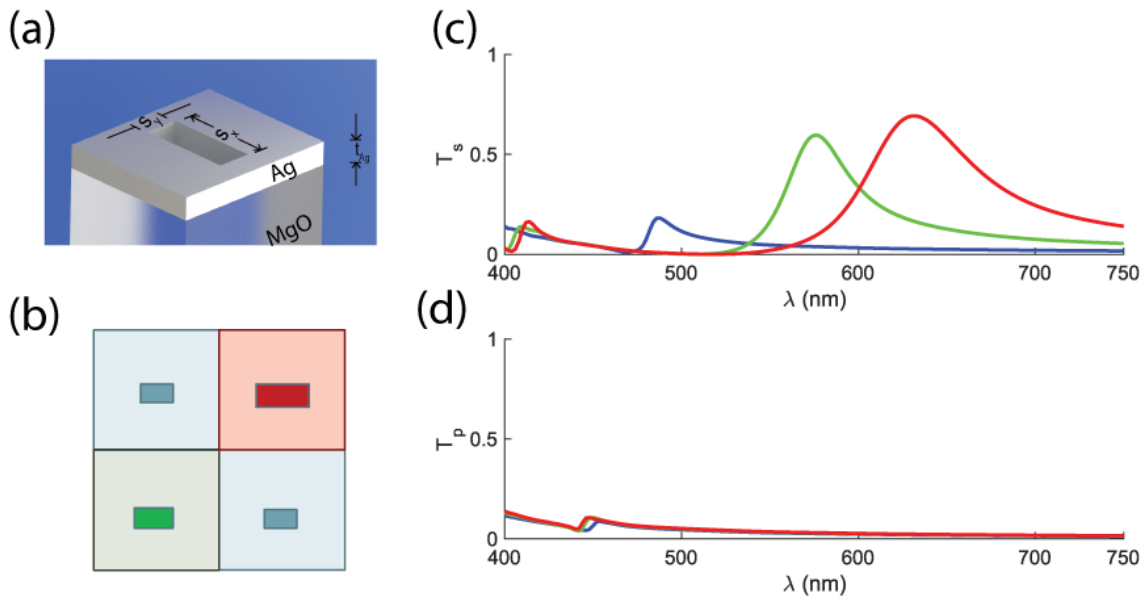


Figure 3.2 (a) 3D Illustration of a unit cell for a color. (b) Proposed supercell containing unit cells of each color. Blue, Green, and Red colored rectangle represent their respective slits with desired resonant frequency (c)  $s$ -polarized and (d)  $p$ -polarized transmission coefficient simulated for three different slit lengths, blue, green, and red represent three different lengths of the slit.  $S$ -polarization is defined when light is polarized parallel to the slit ( $x$  direction in (a)) and for  $p$ -polarization it is perpendicular to the slit ( $y$  direction in (a))

For each set of amplitude and phases, the entire image can be reconstructed at the same distance with the availability of point sources of the same magnitude and phase. Now, to generate a color

hologram at an image plane, the amplitude and phase of each color components should be calculated at the wavefront plane. Accordingly, if the point sources are introduced with same amplitude and phase as the colors at the wavefront plane, it is possible to reconstruct the initial image at the virtual image plane.

### 3.4 Unit-cell design for metasurface hologram

We used a nanoslit-based metasurface to provide the necessary phase modulation to create the metasurface. The transmission peak of a complimentary nanoslit antenna can be tuned by adjusting the antenna length. Figure 3.1(a) shows a unit cell for a single color, which consists of an MgO substrate with silver. The center part is patterned with a nanoslit, where  $s_x$  and  $s_y$  represent the dimensions of the slit. The slit dimensions are optimized in such a manner that it propagates minimum light for  $p$ -polarized light and maximum light for  $s$ -polarized light. Here,  $s$ -polarization is defined when light is polarized parallel to the slit ( $x$  direction in Figure 3.1(a)) and for  $p$ -polarization it is perpendicular to the slit ( $y$  direction in Figure 3.1(a)). The three-color components, red, green, and blue, are represented by 676 nm, 520 nm, and 488 nm wavelength, respectively.

For a film thickness of  $t_{Ag} = 50$  nm and  $s_x = 30$  nm, the dimensions of the slits representing different colors were  $s_y = 40$  nm for blue,  $s_y = 60$  nm for green, and  $s_y = 110$  nm for red color. Since the blue slit resonance is weaker compared to the green and red slit resonances, twice the number of blue slits are used to represent each color point. Figure 3.1(b) shows the illustration of a complete super-cell representing one complex amplitude and phase of a point with three colors. The red, green, and blue colors represent the position of red, green, and blue unit cells within the super-cell. Figure 3.1(c) and Figure 3.1(d) show the  $p$ -polarized and  $s$ -polarized transmission coefficients of individual slits. Each unit cell shows the transmission resonance at the designed wavelength for  $s$ -polarized and minimum  $p$ -polarized transmission. The amplitude obtained by each antenna is fixed, while the phase can be adjusted by rotating the antennas. For our color hologram-generating scheme, we should use a binary amplitude modulation scheme and an arbitrary phase modulation scheme. In practice, the phase modulation of the angles is limited by the fabrication tolerance of the structures. Rotating each of the apertures causes each antenna to introduce a geometric phase to the propagating light beam.

### 3.5 Material Characterization

We use epitaxial silver thin films grown on MgO substrate to fabricate the metasurface. The thin film is characterized with a VASE ellipsometer to obtain the optical constants.

Figures 3(a) and Figure 3(b) show the real and imaginary part of the electric permittivity of the silver film grown on MgO and it is compared to recently published works[114], [171] on epitaxial silver thin films grown on silicon-111 and reported thicker silver films[172], [173]. Our silver film shows the lowest loss compared to other silver films of equivalent thickness, grown on a transparent substrate. The deposited film shows a comparable loss at blue wavelengths while losses peak at red wavelengths comparing to the recent works. The thickness of the grown film is only 50 nm and is quite suitable for producing a metasurface to manipulate light. Figure 3(c) shows the AFM measurement of the silver surface. The grown film is ultra-smooth, with an RMS roughness  $R_a$  of 0.318 nm. Figure 3(d) shows the TEM measurement of the film (FFT shown in the inset).

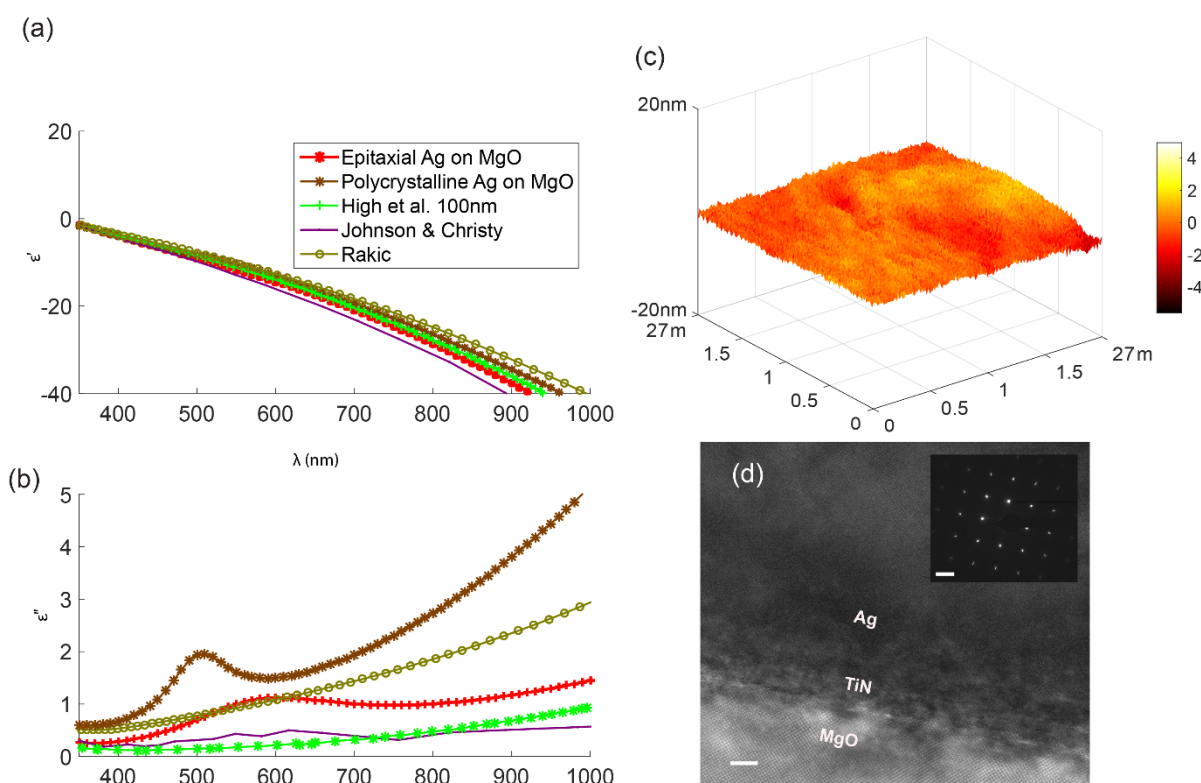


Figure 3.3 Optical Properties and AFM image of the silver on MgO - (a) real and (b) imaginary part of permittivity of the silver film. (c) AFM measurement of surface roughness profile of the silver film. (d) TEM measurement of the silver film. Scale bars represent 5 nm

A 50nm thin silver film with Ge wetting layer was evaporated on a MgO substrate to compare with the epitaxial film. It has been shown that Ge wetting layer causes surface roughness of silver film to reduce significantly. [174] Figure 3.4 shows XRD counts for the two different silver films. The inset shows the zoomed in XRD peak for silver for the epitaxial silver film deposited with TiN wetting layer. Silver-deposited with the wetting layer shows no XRD peak.

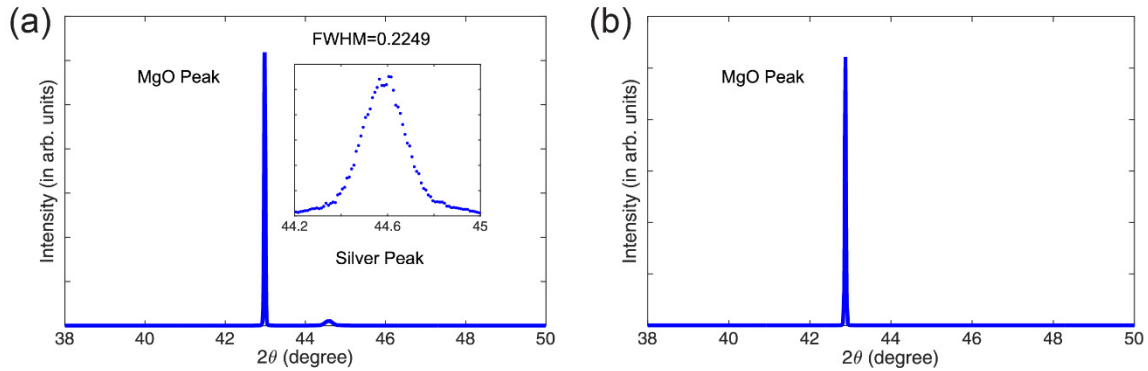


Figure 3.4(a) XRD counts of Epitaxial Silver film on MgO substrate. Inset shows the magnified silver peak (b) XRD counts of polycrystalline silver film

The grain sizes are determined using the Scherrer equation [175]

$$\tau = \frac{K\lambda}{\beta \cos \theta} \quad (3.2)$$

, where we use shape factor,  $K = 0.9$ , x-ray wavelength,  $\lambda = 1.54059 \text{ \AA}$ , Full-width Half Maximum of the peak,  $\beta = 0.2249^\circ$ , Bragg angle,  $\theta = 44.5836^\circ$ . The grain sizes for the 50-nm silver film were found to be around  $\tau = 496 \text{ \AA}$ .

To further demonstrate the crystallinity of the silver film, the sample of silver thin film with Ge wetting layer and 50-nm silver film with 4-nm TiN layer were both characterized using a Transmission Electron Microscope. Both the Silver and TiN layers are epitaxial. Figures S2 (a) and (b) show the TEM images of the sputtered silver film with TiN layer. Figures S2 (c) and (d) show TEM images of the silver film with Ge layer. From the TEM analysis, it is evident that both the silver and TiN thin films are epitaxial.

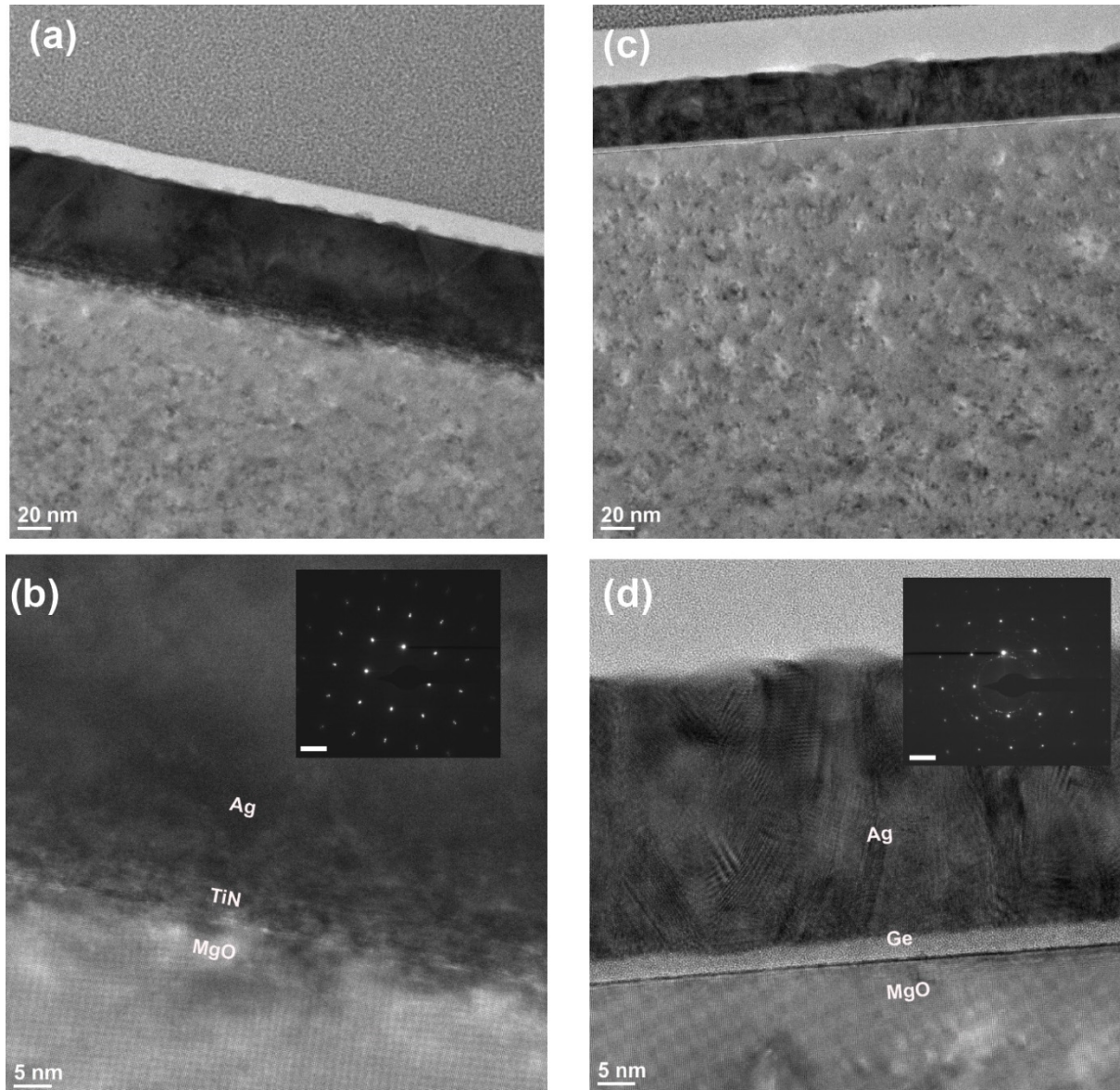


Figure 3.5 TEM image of (a)-(b) silver film with TiN wetting layer and (c)-(d) silver film with Ge layer. Insets in (b) and (d) show FFT post-processing

### 3.6 RGB Component Colors with Metasurface

A sample image with PURDUE written with red, green, and blue colors was taken. Figure 4(a) shows the input bitmap image. The amplitude and phases of the wavefront at a  $5\mu\text{m}$  distance are calculated for a periodicity of  $360\text{ nm}$ , assuming point sources as the bitmap pixels. These point sources are used to generate the three component colors with the metasurface.

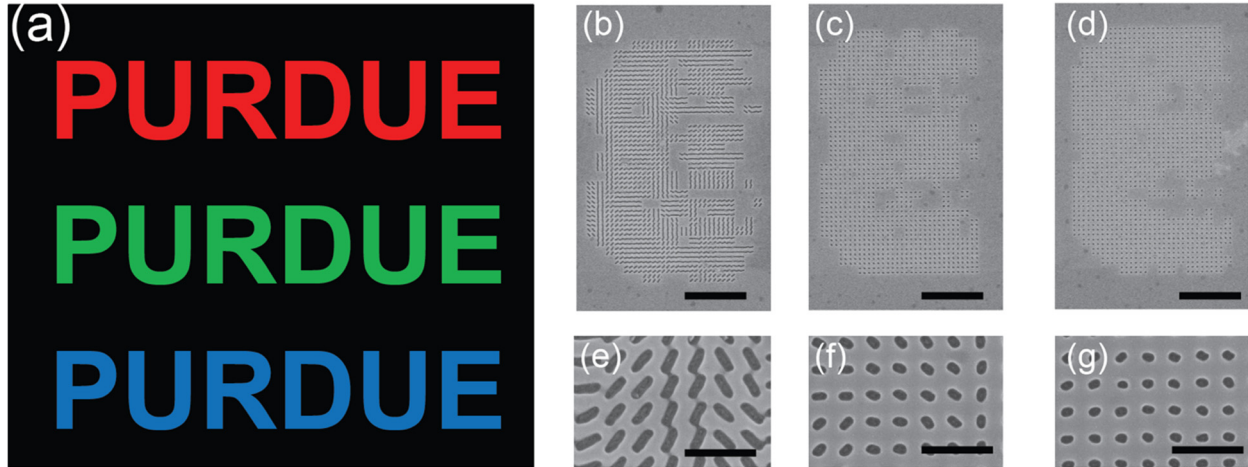


Figure 3.6 (a) Input image for the fabricated metasurface. (b)-(g) SEM Images of the fabricated metasurface structures. (b)-(d) scale bar  $2.5\mu\text{m}$ , (e)-(g) scale bar  $500\text{ nm}$ . (b)-(e) show antennas for red color, (c), (f) show antennas for green color and (d), (g) show antennas for blue color.

The field of exposure of the FIB restricts accurate reproduction of the slits. The total length of the pattern is limited to  $10\mu\text{m}$ . Therefore, the total area of the metasurface is also limited. To illustrate the concept that three component colors could be generated, unit cells consisting of only individual colors red, green, and blue has been considered. Figure 3.6 shows the input image that was used to design the metasurface. Each letter is assumed to be smaller than a  $10\mu\text{m}\times 10\mu\text{m}$  bounding box. The angular resolution was also limited by the finite grid of the FIB ( $3\text{ nm}$ ) and determined by the ability to resolve two separate angles through rotation of the slit pattern in the finite grid. The average angular resolutions are calculated to be  $2.4172^\circ\pm 1.1883^\circ$ ,  $4.9513^\circ\pm 2.1996^\circ$  and  $7.4687^\circ\pm 3.1078^\circ$  for red, green, and blue slits, respectively. The simulated transmission in Figure 3.2(c) and Figure 3.2(d) could not be measured experimentally due to the size constraint of the pattern. The amplitude is modulated with a binary amplitude modulation with a threshold of 33%. Thresholding amplitude is a good approximation to represent the wavefront of the image. Each point in the wavefront is represented with the unit consisting of the designed nano-slits rotated as per the geometric phase of the wavefront. The slits were patterned onto the silver film with FEI Ga-ion focused ion beam. It is known that Ga-ion FIB causes contamination to silver films, so some degradation of their performance is expected from the metasurface. Also, due to the smaller feature sizes of the slits, it was difficult to do e-beam lithography and get proper features at such a small scale. Moreover, the FIB writing limits the total dimensions of the pattern area to  $10\mu\text{m}\times 10\mu\text{m}$ . Due to this pattern size limitation, only the simulated transmission spectrum from Figure

3.2 were used to design the metasurface. Figure 3.6(b)-(g) shows an SEM image of the fabricated structures for red, green, and blue portions of the image.

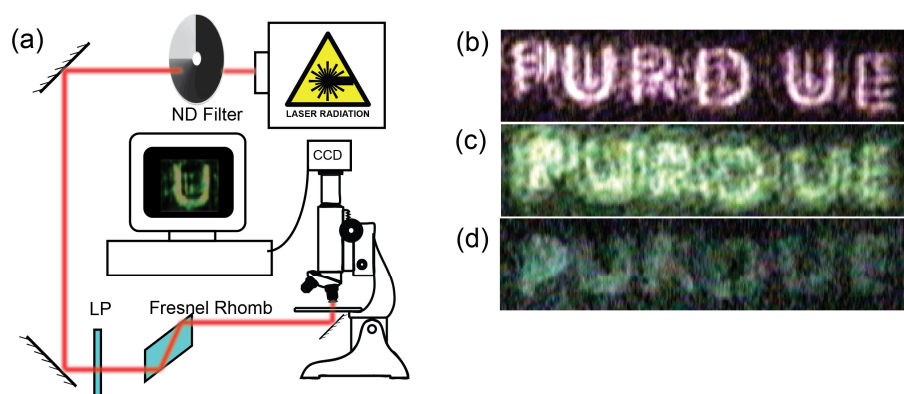


Figure 3.7 (a) Experimental Setup (b-d) Final hologram image captured through CCD camera for (b) red, (c) green, and (d) blue hologram

Figure 3.7 shows the experimental setup for the hologram observation. Collimated beam from an Ar-Kr laser is used as illumination light source. Slit position corresponding to 483 nm, 530 nm, and 647 nm are used for red green and blue light sources respectively. For the white light source, a fiber-coupled NKT-Super K laser source is used. A Raman spectroscopic setup is modified for observing the hologram. Laser illumination is attenuated with a variable neutral density (ND) filter and passed through a broadband linear polarizer (LP). A Fresnel Rhomb is used to convert the linear polarized beam into circular polarized beam, and the sample is illuminated by the output from the Fresnel Rhomb from the bottom. The hologram is observed by focusing the microscope at  $10\mu\text{m}$  above the sample plane using a 50x objective and observing the hologram using a CCD camera.

An Ar-Kr laser light source is circularly polarized and is illuminated on the sample from the transmission side. The microscope stage is moved in precision to  $5\mu\text{m}$  above the surface of the film to observe the holographic images shown in Figure 5(b), which successfully resolves the three-color components. The observed blue color is more red shifted. This could be attributed to the fabricated apertures being larger than the designed nano-slits for blue color. To illustrate the formation of the hologram at the focal plane, we focused the surface of the patterned silver film with the microscope and gradually rotated the focusing knob to translate the stage in z direction at the micrometer scale. Figure 3.8 shows the camera image for each focusing plane. The hologram

image is observed to be sharpest at the designed distance of  $5\mu\text{m}$ . The camera software causes automatic correction to the contrast and brightness of individual color components. This caused slight variation of image color in the final output. Blurring of the images can be attributed to the finite grid size and angular resolution discontinuity.

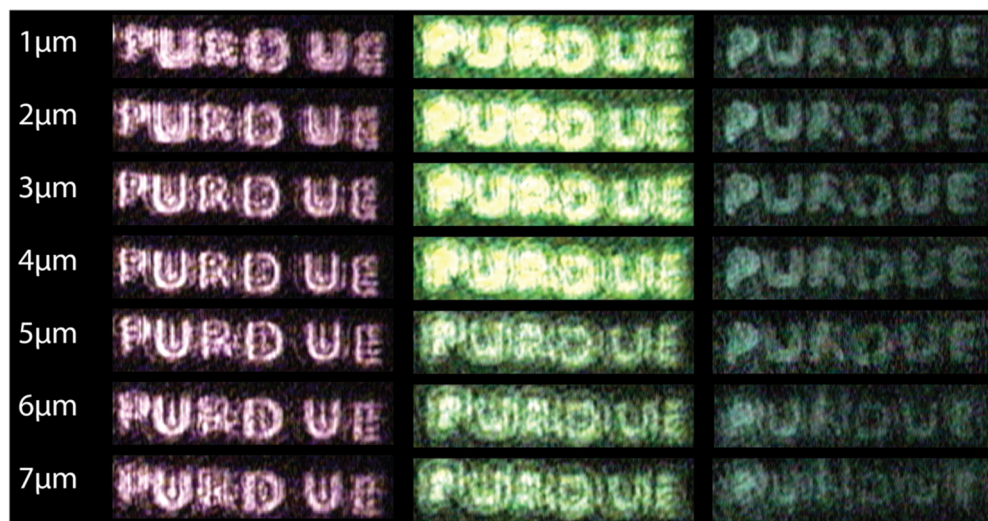


Figure 3.8. Hologram observation by change of focus of the microscope. Left column shows the distance of the focal plane of the microscope set from the surface of the silver film. Each row corresponds to the focal plane for the hologram color

### 3.7 Summary

A hologram generated by a plasmonic metasurface fabricated on ultra-smooth low-loss silver film is demonstrated experimentally. The total thickness of the silver layer is 50 nm, and this is the thinnest metasurface hologram demonstrated in transmission mode. The metasurface is developed by manipulating the Pancharatnam Berry phase of incoming light. The low loss silver based metasurface can work in transmission mode and manipulate light at ultra-thin thickness. The designed nano-apertures work well in the visible region and can produce a three-color image at a virtual imaging plane. The fabrication procedure developed can be utilized in future applications of plasmonic metasurfaces such as vortex beam generation, polarization conversion, bio-sensing, and paves the way to new applications of polychromatic plasmonic metasurfaces in the visible regime.

## 4. IMAGING PLASMONIC HEATING OF METASURFACE

### 4.1 Introduction

Plasmonic metasurfaces are inherently lossy compared to their dielectric counterparts. The loss of the metasurface could be, in turn, converted to applications in different fields such as optofluidics and particle manipulation[176], photo-thermal therapy for cancer treatment [177], thermos-photovoltaic applications[178], heat-assisted magnetic recording (HAMR)[179]. The current temperature scheme measurements due to plasmonic heating include contact measurements, such as scanning thermal microscopy [180], phosphor excited thermal microscopy[181] or probing refractive index change with optical microscope [182]. Existing methods of temperature measurement have limitations in measurement, such as the spatial uncertainty in measurement due to averaging of the index, using specific excitation material (phosphor) and difficulty in measurement in air. Near-field scanning optical microscopy is inherently slow and contacted measurement technique.

The work described in this chapter introduces Time Domain Optical Pump-Probe Thermo-reflectance imaging. The method utilizes reflection change of material due to temperature change, to measure temperature. The scheme could be further utilized to model temperature distribution in a smaller scale or be used to model temperature profile of arbitrary shapes. [183]

### 4.2 Theory of Time Domain Thermo-reflectance

It was shown in the late sixties that the temperature effects optical constants of metal heated by laser radiation [184]. The reflectivity  $R$  of a material depends on temperature, and the first order approximation of temperature dependent reflectivity at  $T_0 + \Delta T$  temperature can be modeled as follows,

$$R(T_0 + \Delta T) \approx R_0 + \left. \frac{dR}{dT} \right|_{T_0} \times \Delta T \quad (4.1)$$

where  $R_0$  denotes the reflectivity of a material at  $T_0$  temperature. Within the linear limit, the temperature of an object can then be estimated by the rate of change of reflectivity. The derivative of reflectivity with respect to temperature is defined as the thermo-reflectance coefficient,

$$C_{\text{TR}} = \left. \frac{dR}{dT} \right|_{T_0} \quad (4.1)$$

Then, for any given material, if the thermorefectance coefficient is known, the temperature change can be easily related to the reflectivity change of the material as,

$$\Delta T(x, y) = \frac{\Delta R(x, y)}{C_{\text{TR}} R_0} \quad (4.3)$$

Thermo-reflectance coefficient  $C_{\text{TR}}$  can be measured by calibrating a sample with controlled temperature rise and measuring temperature with an alternative direct high-precision technique.

### 4.3 Methods

#### 4.3.1 Measurement Technique

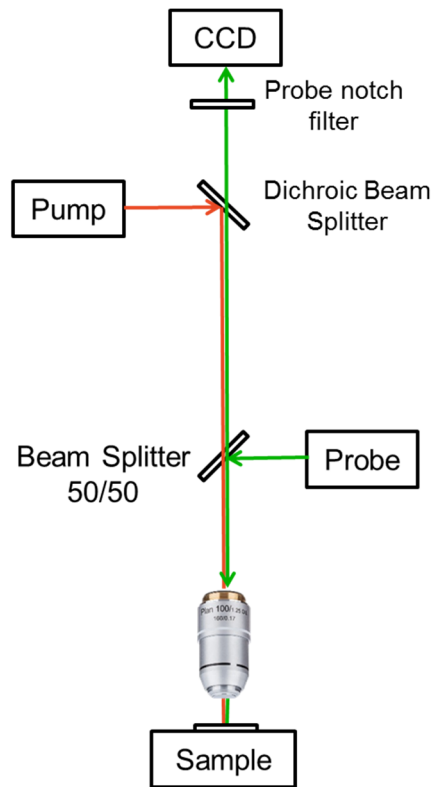


Figure 4.1 Experimental setup for Time Domain Thermo-reflectance

The measurement of the temperature rise due to plasmonic heating was done using a time-domain thermo-reflectance method. An 825-nm continuous-wave diode laser coupled to a single mode

fiber was used as an excitation source. The laser was chopped to 1 ms 20% duty-cycle pulses. The laser was tightly focused using a lens at the pump port, to one-micron diameter spot-size onto the sample. For probing the reflection change, an LED with emission wavelength centered at 530nm is used, with a full field of view. The pump beam is collimated from the fiber using a collimator lens, and using a short-pass dichroic beam splitter, reflected onto the sample through the objective. The dichroic beam splitter reflects light with wavelength larger than 800 nm and transmits light with a wavelength less than 800 nm, thereby reflecting the pump and transmitting the probe pulse. A 50/50 beamsplitter is used to reflect the probe onto the sample through the microscope objective and again, through the CCD detector.

### 4.3.2 Sample Preparation

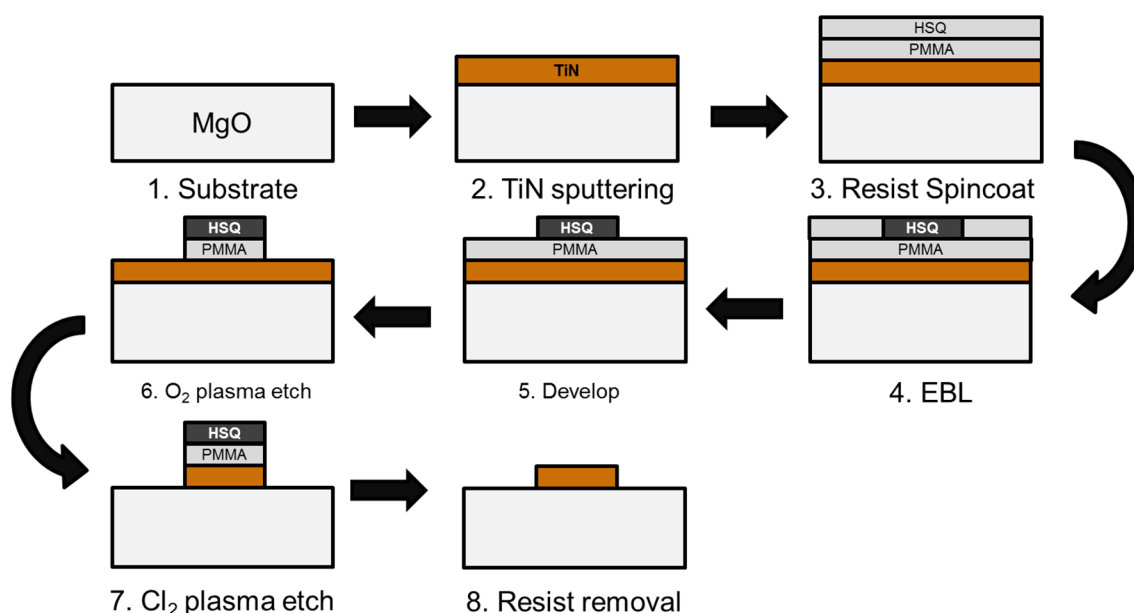


Figure 4.2 TiN nanodisk array sample preparation.

Titanium Nitride (TiN) nanopillar array was prepared by patterning an epitaxially grown TiN thin-film. A 100nm TiN film was grown on a MgO substrate using RF magnetron sputtering. Negative e-beam resist HSQ needs to be used to fabricate disk structures. Since HSQ removal process requires hydrofluoric acid (HF) that damages the substrate, a sacrificial PMMA layer is used. PMMA 950 A2 resist layer was spin-coated at 1000rpm for 1 minute and baked at 160°C for 5 minutes. XR-1541-006 (HSQ) resist was spin coated at 1500rpm for 1 minute and baked at 80°C for 4 minutes. Patterns were exposed with a Vistec VB6 Electron Beam Lithography (EBL)

machine. After exposure sample was developed using 25% Tetramethyl Ammonium Hydroxide (TMAH) solution for 30 seconds and rinsed with DI water for 1 minute. Using the developed HSQ as mask, the PMMA layer is etched with oxygen plasma (flowrate 15 sccm, pressure 0.6 Pa, forward power 80 W, and bias power 60 W). The TiN layer acts as an etch stop layer for the oxygen etch. Next, the TiN thin film is etched using an Inductively Coupled Plasma Reactive Ion Etcher (ICP-RIE) with  $\text{Cl}_2$  gas flow rate 26sccm, pressure 0.8 Pa, Forward Power 150 W, and Bias Power 30W and etch time of 8 min. Here the MgO substrate acts as the etch stop layer. After the etching, the resist is removed by submerging the sample overnight in heated PG Remover solution, and 20-minute sonication in PG Remover. The PMMA underlayer is completely dissolved, removing the HSQ as well. The sample is then washed acetone and isopropanol rinse and  $\text{N}_2$  blow dry. Figure 4.4 shows the different steps of fabrication process.

### 4.3.3 Thermoreflectance of Survey of samples

An array of multiple samples with varying periodicity and diameter of disks is prepared to showcase the capability of the technique for rapidly measuring temperature and characterize samples.

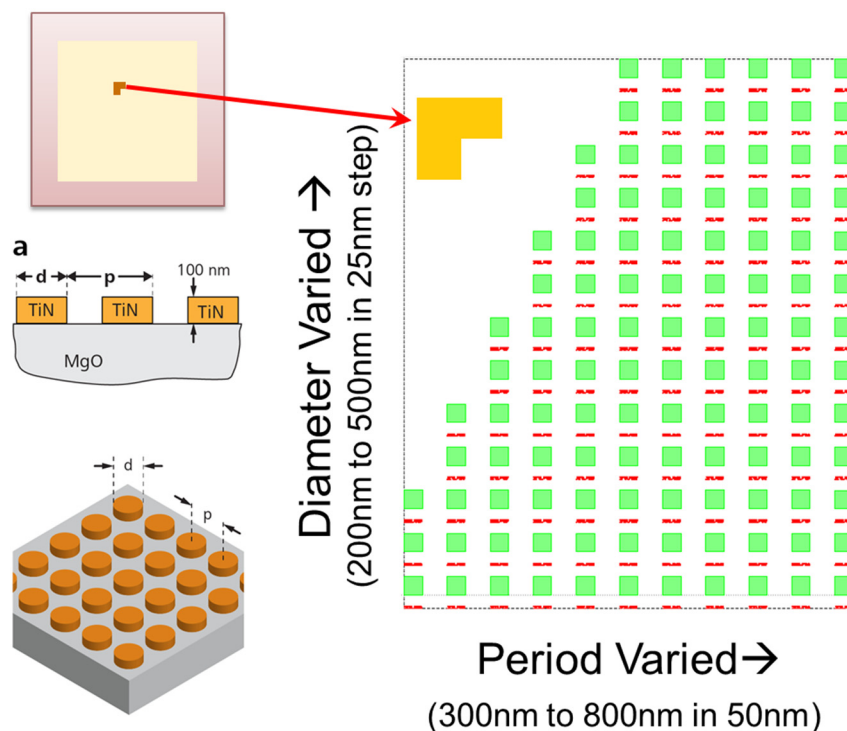


Figure 4.3 Sample survey layout. Block diagram in right shows the diameter and periodicity variation in the sample. In y-direction, diameter is increased in 25 nm steps from 200 nm, and in x direction, the period is increased from 300 nm in 50 nm steps

Figure 4.3 shows the layout of the sample preparation for the temperature rise survey. The sample was prepared with multiple  $100 \times 100 \mu\text{m}^2$  arrays with disk diameter varied from 200nm to 500nm in 25nm steps, and period varied from 300nm to 800 nm in 50 nm steps, minimum gap size between particles is always considered to be 50nm.

#### 4.4 Results

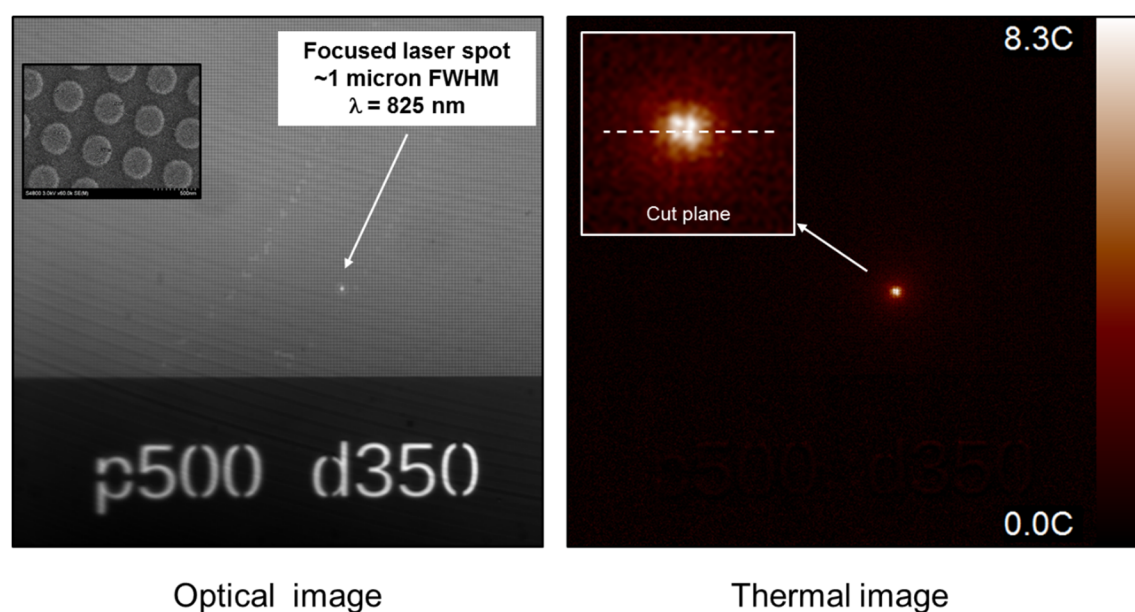


Figure 4.4 Comparison between optical image and obtained thermal image

The pump spot is visible optically through the microscope by removing probe notch filter. Left panel of Figure 4.4 shows the pump spot captured through the CCD camera and the corresponding thermal profile obtained through thermoreflectance imaging. Figure 4.5 shows the comparison of thermoreflection between patterned and unpatterned film. For the patterned film, a disk array of 200nm diameter and 350nm period is used. At the center of the plot maximum temperature rise for the patterned array becomes 24K, where temperature rise for the unpatterned film remains 3.5K. The temperature rise also is linearly proportional to the input pump power, where the disk array has more temperature rise than the unpatterned film, as shown in Figure 4.5(c).

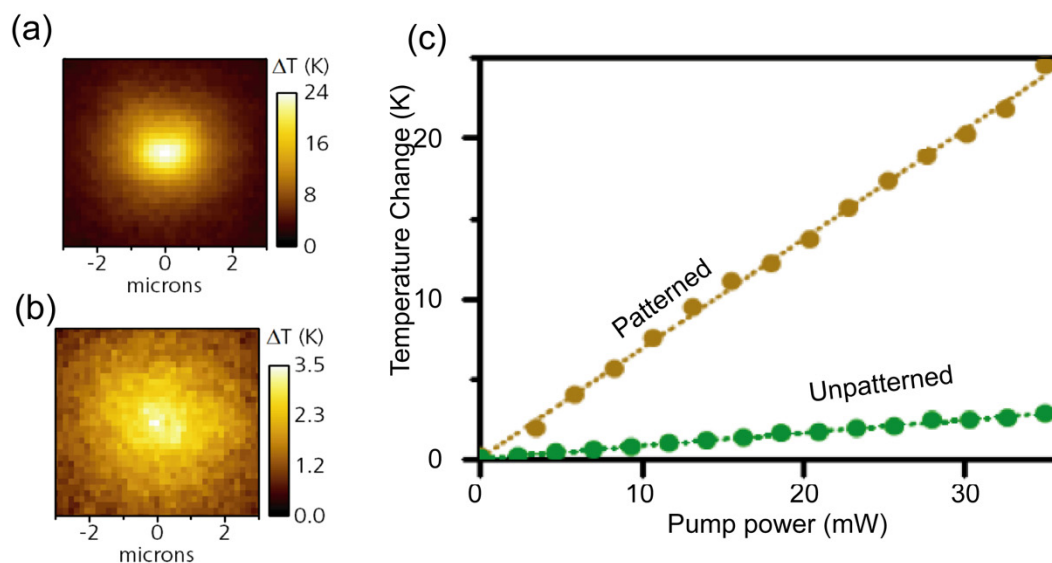


Figure 4.5 Temperature rise of patterned films: thermoreflectance of (a) patterned (b) unpatterned film, (c) temperature change as a function of pump power and (d) thermoreflectance image of the unpatterned film.

For the different diameter and period combinations illustrated in Figure 4.3, the thermoreflectance image is obtained for each array.

To avoid the possible reflection change due to the change in the filling factor, the thermoreflection coefficient for each array is first determined through calibration process. The samples are heated with a Joule's heater, and the thermoreflection coefficient is calculated by measuring the change in reflection and the measured temperature. The optical-thermoreflectance imaging (OTI) is performed with the experimental setup shown in Figure 4.1. The resulting temperature change is measured in steady state by time-averaging the reading, Figure 4.6(a) shows the temperature rise for selected 56 samples from the survey. To demonstrate the effect of plasmonic heating on the temperature in the array, only the arrays which exhibit a temperature rise of more than  $1^{\circ}\text{C}$  from the bare-film is shown. Figure 4.6(b) shows simulated result of optical absorption assuming periodic boundary condition and an infinite array. It may be mentioned that the spot size for the measurements in the Figure 4.6(a) is  $1\mu\text{m}$ , and can only illuminate the array in a Gaussian profile.

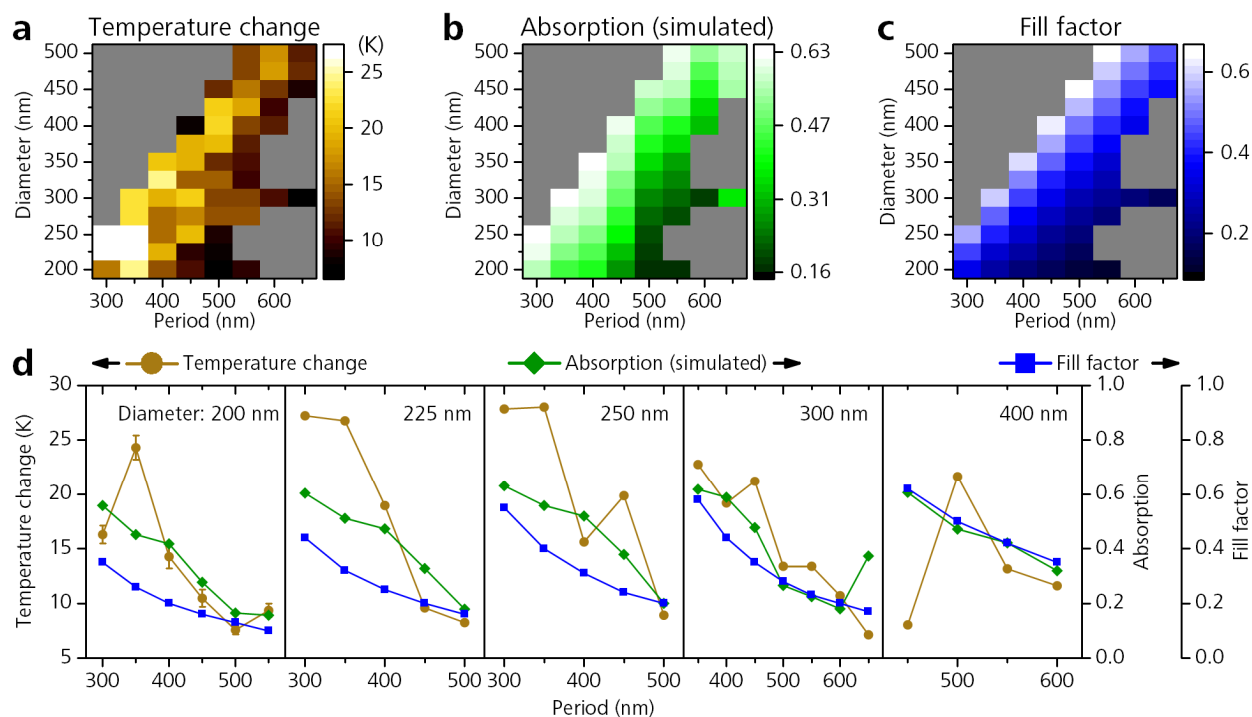


Figure 4.6 (a) Thermal map for the survey as measured, (b) simulated optical absorption of the array assuming periodic boundary condition, (c) fill factor of each array element. [183] (d) temperature change maxima shown for different array geometries, with simulated absorption and fill factor of each array

## 4.5 Arbitrary Temperature Profile Mapping

A scheme based on the survey of temperature rise result is proposed here, to arbitrarily shape the temperature profile by adjusting the diameter and period of optical absorbers. Since the temperature rise strongly depends on both the periodicity and diameter of the plasmonic structures, the temperature profile could be engineered by modifying the periodicity and diameter of an array.

## 4.6 Summary

In summary, this is the first reported thermoreflectance imaging of temperature rise due to plasmonic heating. Heating by laser spot illumination could be imaged at optical diffraction limit. The measurement technique illustrates fast and non-contact characterization of temperature rise due to plasmonic heating and can be used to optimize designs and accurately model temperature rise due to optical heating.

## 5. REFRACTORY PLASMONIC METASURFACE FABRICATION FOR THERMO-PHOTOVOLTAIC APPLICATION

### 5.1 Introduction

Thermal to photovoltaic energy conversion can be obtained by selectively converting heat energy to emitted radiation at a wavelength. The radiation is then absorbed by a photovoltaic (PV) cell that converts it to an electromotive force to drive external current through a circuit. The inherent small footprint of plasmonic metasurfaces can be used to convert heat to thermal radiation efficiently. A solar absorber can be combined with the emitter to convert solar energy first to heat and then to the selective radiation band corresponding to the PV cell. Recently it has been theoretically predicted that by judiciously tailoring the spectral properties of the emitters and absorbers components using metasurfaces, the efficiency for direct energy conversion from solar/thermal energy to electricity could potentially reach an unprecedented value of  $\sim 85\%$  [185]. This estimated theoretical efficiency is in striking contrast to the current physical limitation ( $\sim 30\%$ ) imposed by the Shockley-Queisser limit [186] for a single silicon p-n junction cell [187]. The development of optical MS structures would open new frontiers for realization of solar thermophotovoltaic and thermophotovoltaic systems. Both systems require metasurface elements operating at a very high temperature ( $> 1000^\circ\text{C}$ ). Part of this chapter is published in [188] and reused with permission.

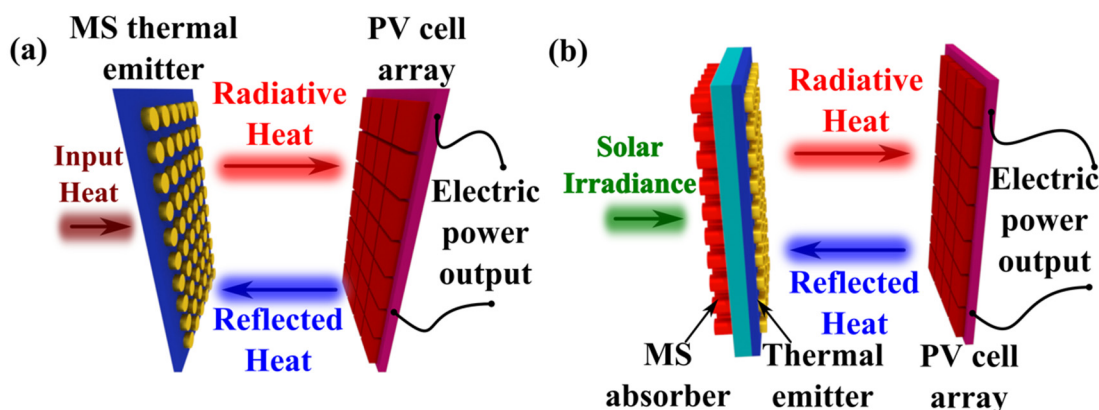


Figure 5.1 Thermophotovoltaics concept (a) Thermophotovoltaic configuration, using external heat source to generate radiative heating and (b) Solar Thermophotovoltaic configuration where solar irradiance is used for generating heat

### **5.1.1 Thermophotovoltaics (TPV):**

In a TPV system, thermal radiation is directly converted to electricity via the photovoltaic (PV) effect. A TPV system consists of a PV cell array and a selective emitter with the emissivity matching absorption band of a PV cell. A schematic of a TPV system is shown in Figure 1(a). TPV energy conversion offers numerous significant advantages over competing technologies [189], [190]. These include the realization of highly versatile, modular, low-weight, and compact electric generators (portable or stationary), which are noiseless, low-maintenance, and energy-efficient [191]. Optimal TPV energy conversion requires large area metasurface emitters (see, Figure 1(a)). Hence, robust refractory materials, which are compatible with low-cost, large-area fabrication-techniques, are critical for practical highly efficient metasurface TPV elements.

### **5.1.2 Solar thermophotovoltaics (STPV):**

An STPV system comprises an absorber, an emitter, and PV cells, as shown in Figure 1(b). The absorber, heated by concentrated solar energy, increases the temperature of the emitter, which is engineered to radiate within the specific band where the absorption of a PV cell is at its maximum. Hence, by absorbing broadband solar energy and then re-emitting it within a desired working band of the PV cell array, the MS-based STPV architecture provides an efficient way of harvesting solar energy [187].

## **5.2 Current and Future Challenges to incorporate TPV**

The inherent ability of MSs to tailor the absorption/emittances of optical surfaces is of great interest in TPV and STPV. The functionality of MSs can be further enhanced by designing emitters that operate at elevated temperatures and match the spectrum of solar radiation, thus maximizing the absorption. MS resonant super-absorbers have already demonstrated polarization-independent absorption in the entire visible spectrum [91]. The absorption/emission can also be engineered to match that of energies emitted by other forms of radiative emitters, such as a nuclear reactor, engine, or combustion chamber [192]. Plasmonic metasurface emitters for STPV and TPV require materials that maintain good optical properties at high-temperatures and field intensities [193]. Conventional noble metals (Au and Ag) have low melting points and damage thresholds. Nanostructuring these materials further decreases the maximum temperature that they can withstand. At high temperatures, gold MSs were shown to deform [106]. Passivation with a dielectric was shown

to improve the performance of gold MSs at high field intensities [194]. While TiN is CMOS compatible, many of the processes used to grow TiN involve the use of lattice matched substrates and high temperatures, which limits its practical applicability. The material also oxidizes at elevated temperatures, which makes it important to passivate with a suitable capping layer [194]. There have been few investigations on the high-temperature properties of thermally stable dielectric capping layers. As refractory plasmonic materials are inherently robust, they often require special growth conditions to reduce optical losses and require sophisticated etch chemistry for patterning. A new material platform would also require the characterization of high-temperature optical properties to design, the MS structures for different applications. The optical properties of a material are heavily dependent on different growth conditions and crystal properties [195], which necessitates further optimization for the best plasmonic response. Material research is needed to explore possible refractory materials that would have comparable optical properties to Ag and Al. Also, for any new material platform there is the challenge of developing a scalable patterning recipe.

### **5.3 Material Platforms for TPV**

#### **5.3.1 Conventional Refractory Materials**

With the advent of new material research, alternatives to noble metals were explored for plasmonics. The first choices for replacing them were high melting point metals such as platinum (Pt) and tungsten (W). The lower real-part of the permittivity and the higher losses of refractory materials compared to noble metals are usually compensated with gap-plasmon structures. Pt was explored as a candidate for TPV emitters, with a Pt disk resonator and an alumina spacer which can withstand heating cycles of up to 650°C [196]. Recently, Pt nano-disk array is used to demonstrate up to 24% thermal to electric conversion efficiency [197]. High-temperature applications with W were also explored for TPV. Gap-plasmon structure with a SiO<sub>2</sub> spacer [198] and W gratings with a SiO<sub>2</sub> protective film [199] showed suitable emission properties from 400 nm to 2000 nm wavelength range.

#### **5.3.2 Refractory transition metal nitrides**

Titanium and zirconium nitrides (TiN and ZrN) are promising alternatives to these high loss materials and demonstrate superior optical functionality at high temperatures. Though they exhibit

higher losses compared to Au or Al, they can withstand significantly higher temperatures [96]. A broadband absorber has been demonstrated using a bilayer TiN/SiO<sub>2</sub> and patterning the top TiN into square-shaped loop shapes. The structure has shown a higher damage threshold and stability to annealing compared to a similar structure made with gold [106].

Moreover, recent studies indicate that temperature-dependent optical properties of epitaxial TiN degrade at a much lower rate with increasing temperature compared to Au or Ag [200]. Also, fabricated epitaxial TiN-based nanodisk arrays show a broader optical absorption and a better tolerance to diameter variation [107]. Multi-objective optimization of TiN nanohole MSs, generating arbitrary far-field optical patterns, has been demonstrated using an evolutionary algorithm [201]. Refractory ZrN has been patterned to prepare a photonic-spin-hall-effect (PSHE)-based MS for spectroscopic application [108].

### **5.3.3 Passivating refractory layers**

Noble metals have already been reported to be used in absorbers with protective capping layers that enhance their stability. With a 4-nm passivating alumina layer, noble metals can withstand a temperature of up to 800°C [194]. With annealed deformation of a gold film, gold islands were formed on alumina and indium doped tin oxide (ITO), and the resulting structure has been used to make emitters at 900°C with 22-hour long exposures in an oxidizing environment [202]. Alumina-passivated Pt disks can be heated up to 1055°C and have reported a power conversion efficiency of 24% [197]. With these results, the use of passivating refractory nitrides with matching refractory ceramics shows further promise of increasing the damage threshold and robustness of the structures [203].

## 5.4 Fabrication process for TiN based TPV emitter

### 5.4.1 Design Process

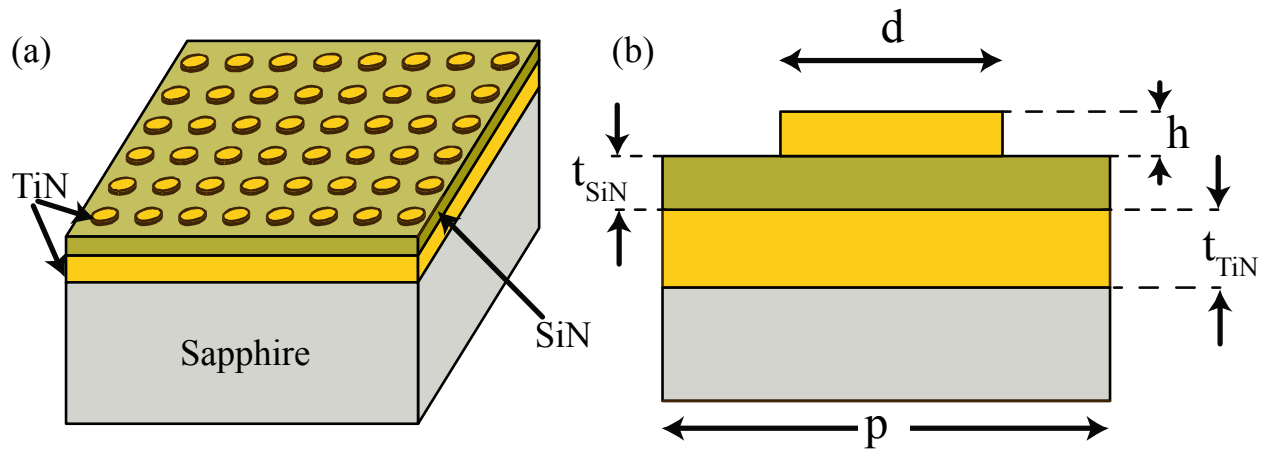


Figure 5.2 TPV prototype schematic and modeling (a) schematic of TPV array showing different layers (b) cross-sectional view of a single unit cell

TPV emitter design TiN is explored here. Gap-plasmon structures with TiN back reflector, SiN spacer, and TiN resonator disks are used for TPV emitter structure fabrication (as shown in Figure 5.2 (a)). The structure is optimized for maximum emission in the bandgap of the photovoltaic cell, and minimum emission in the out of band wavelengths. Parameter space consists of the of disk diameter,  $d$ , periodicity,  $p$ , disk height,  $h$ , spacer thickness,  $t_{SiN}$  and TiN film thickness  $t_{TiN}$ . The optimization procedure is elaborated [204] and based on the particle swarm optimization; the following parameters are obtained  $d = 100\text{nm}$ ,  $p = 165\text{nm}$ ,  $h = 30\text{nm}$ ,  $t_{SiN} = 48\text{nm}$ ,  $t_{TiN} = 150\text{nm}$ . To prepare the material stack, first, a TiN film of 150nm thickness is deposited epitaxially on to a sapphire substrate using RF sputtering. SiN film of 48nm thickness is deposited on top of the TiN layer using LPCVD nitride furnace. After deposition of each layer, the layer stack is characterized with VASE ellipsometer. Figure 5.3(a) and Figure 5.3(b) show the fitted real and imaginary part of the permittivity of TiN. The bottom TiN is lattice matched with the sapphire substrate. However, the SiN layer is amorphous and not lattice-matched with the substrate. Therefore, the 30nm TiN grown on SiN thin film is significantly more lossy and less plasmonic than the epitaxially grown 150nm TiN on sapphire. Figure 5.3(c) and Figure 5.3(d) shows the measured permittivity of the SiN layer.

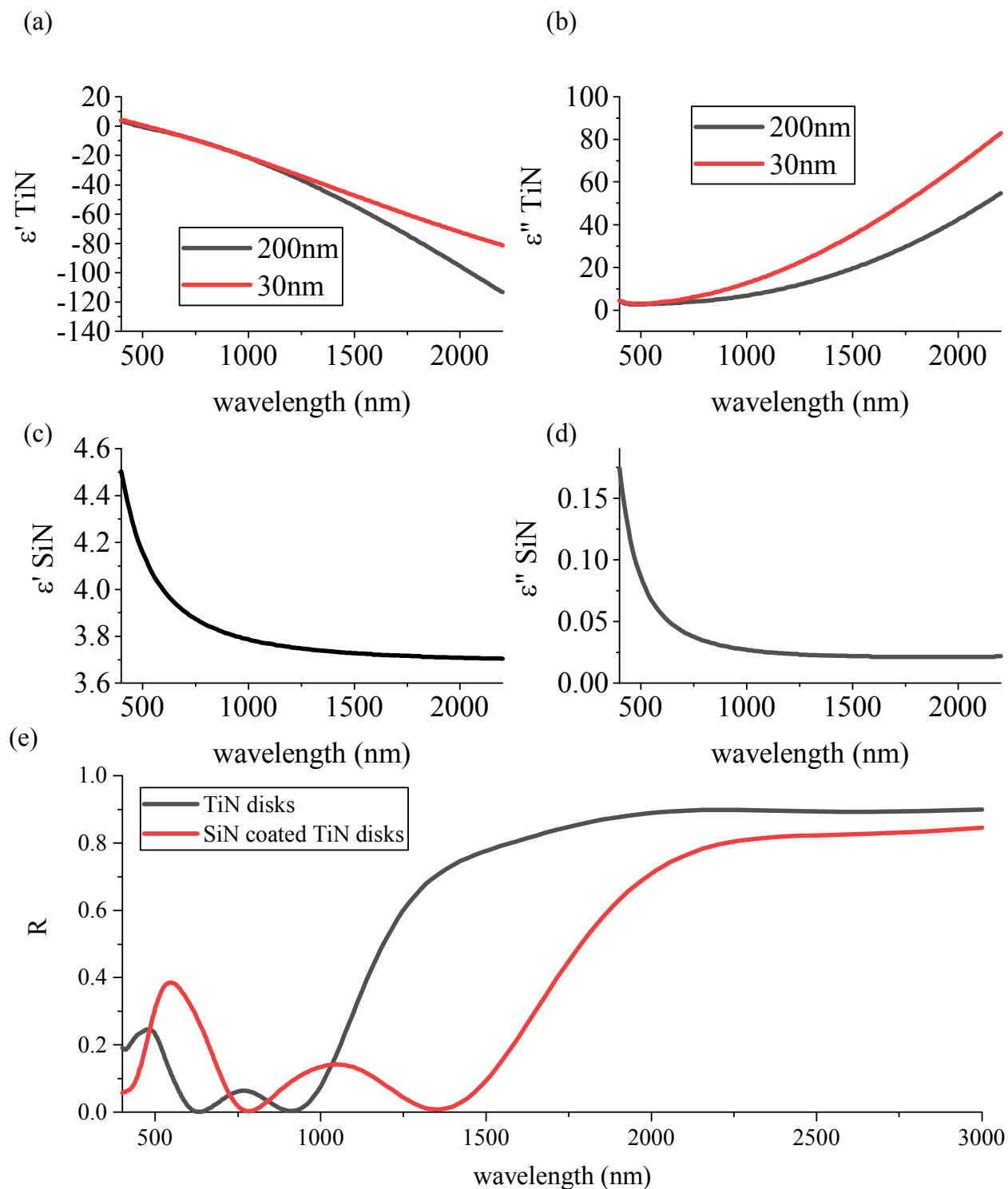


Figure 5.3 Fitted optical constants of TiN, SiN and simulated reflection (a) real part and (b) imaginary part of TiN permittivity for the 200nm and 30nm layers. (c) real part and (d) imaginary part of SiN permittivity (e) FDTD simulated reflection spectra of the unit cell

Both the TiN layers are fitted with Drude-Lorentz model with the complex relative permittivity  $\varepsilon_r(h\nu) = \varepsilon'_r(h\nu) + i\varepsilon''_r(h\nu)$ ,

$$\varepsilon_r(h\nu) = \varepsilon_{r,\infty} + \sum_k \frac{A_k}{E_k^2 - (h\nu)^2 - iB_k(h\nu)} \quad (5.1)$$

The photon energy  $h\nu$  in electron-volts, is related to the wavelength by  $h\nu = \frac{hc}{e\lambda} \approx \frac{1243 \text{ nm}}{\lambda} \text{ eV}$

For the 200 nm TiN layer, the film is fitted with a Drude term ( $A_1 = 46.094 \text{ (eV)}^2$ ,  $B_1 = 0.2547 \text{ eV}$ ,  $E_1 = 0 \text{ eV}$ ) and two Lorentz terms ( $A_2 = 14.821 \text{ (eV)}^2$ ,  $B_2 = 0.5463 \text{ eV}$ ,  $E_2 = 3.428 \text{ eV}$ ,  $A_3 = 6.5214 \text{ (eV)}^2$ ,  $B_3 = 2.312 \text{ eV}$ ,  $E_3 = 2.3153 \text{ eV}$ ),  $\varepsilon_{r,\infty} = 4.544$ . For the 30nm TiN grown on SiN, the film is fitted with a Drude term ( $A_1 = 52.758 \text{ (eV)}^2$ ,  $B_1 = 0.52511 \text{ eV}$ ,  $E_1 = 3.6774 \text{ eV}$ ) and a Lorentz term ( $A_2 = 27.704 \text{ (eV)}^2$ ,  $B_2 = 1.1316 \text{ eV}$ ,  $E_2 = 3.6774 \text{ eV}$ ),  $\varepsilon_{r,\infty} = 5.5529$ . The term  $B_2$ , which is related to the imaginary part of  $\varepsilon_r(h\nu)$ , is higher in the 30 nm film, indicating higher loss.

The unit cell of the periodic disk array can be modeled using the optimized parameters and measured permittivity of the thin films. Lumerical FDTD is used to model the unit cell of the periodic array with Bloch periodicity. Figure 5.3(e) shows the reflection spectra of the TiN disks on top of SiN spacer layer TiN back reflector on a sapphire substrate. The black curve denotes reflection spectra without any SiN overcoat. As a conformal SiN layer of 60nm is added on top of the TiN disks, the spectrum is red shifted (as shown with the red curve), with higher reflection above 1600nm wavelength. This confirms the fitness criteria of the optimization; as for indium gallium arsenide (InGaAs) PV cell, the bandgap energy is 0.75eV and 1657nm corresponding cutoff wavelength. Adding the SiN overcoat increases the reflection peaks inside the band while decreasing the reflection at longer wavelength compared to the bare TiN disk array. This can be explained as the losses incurred in the SiN film, as seen in Figure 5.3(d).

#### 5.4.2 Prototype Fabrication

A prototype sample of TPV emitter is needed to test the emissivity and optimize the design for mass production. The fabrication process is outlined in Figure 5.4. A double side polished sapphire

wafer is used as a substrate. TiN thin film of 150nm is sputtered onto the substrate like the process described in section 4.3.2. The sample is then taken to an LPCVD nitride furnace, and silicon-nitride (SiN) of a predetermined thickness is deposited onto the sample. Then the top layer of TiN is deposited onto the sample. This tri-layer structure is then patterned using electron-beam lithography. A negative e-beam resist is spin coated on top of the trilayer stack and exposed with electron-beam to make the disk structures. After development, the resist is used as a hard mask to etch the TiN. The SiN layer below the top TiN acts as an etch-stop layer. After resist removal, an additional SiN protective layer is deposited.

### 5.4.3 Prototype Characterization

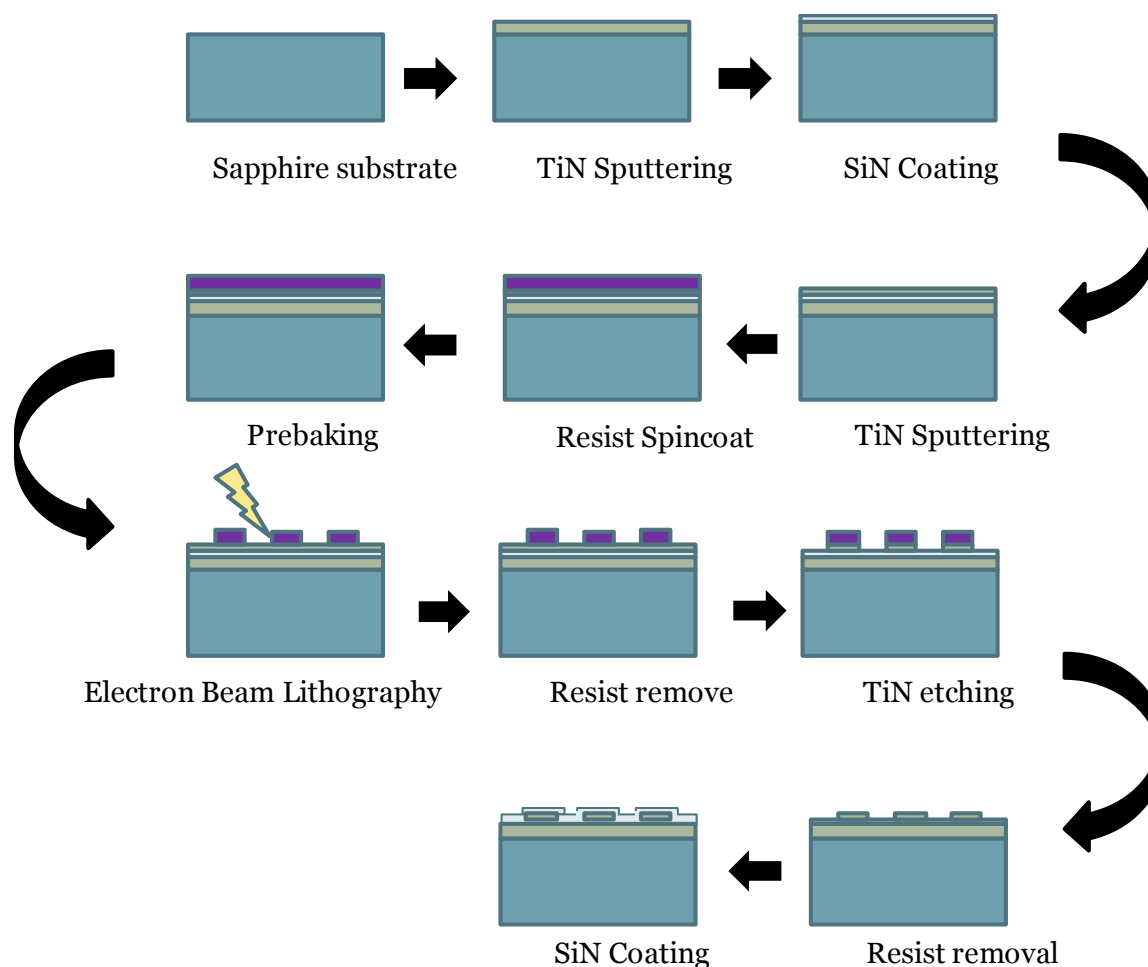


Figure 5.4 Ebeam Prototype fabrication

Small area prototype of the TPV emitter was fabricated with e-beam lithography as mentioned above. Patterns of up to  $2 \times 2 \text{ mm}^2$  could be fabricated with e-beam with around 6 hours of write

time. The negative e-beam resist, Hydrogen silsesquioxane (HSQ) degrades in vacuum over time, and cannot be reliably patterned after 6 hours. Figure shows the SEM image of the fabricated sample. After the exposure, the sample was developed with 25% aqueous tetra-methyl-ammonium-hydroxide (TMAH) for 30s, and rinsed with water. The TiN is etched with inductively coupled plasma reactive ion etcher (ICP-RIE) for 3.5mins in 26sccm  $\text{Cl}_2$  gas with forward power of 150W and bias power of 30W and 0.6Pa pressure. Figure 5.5 shows the SEM image of the fabricated disk array.

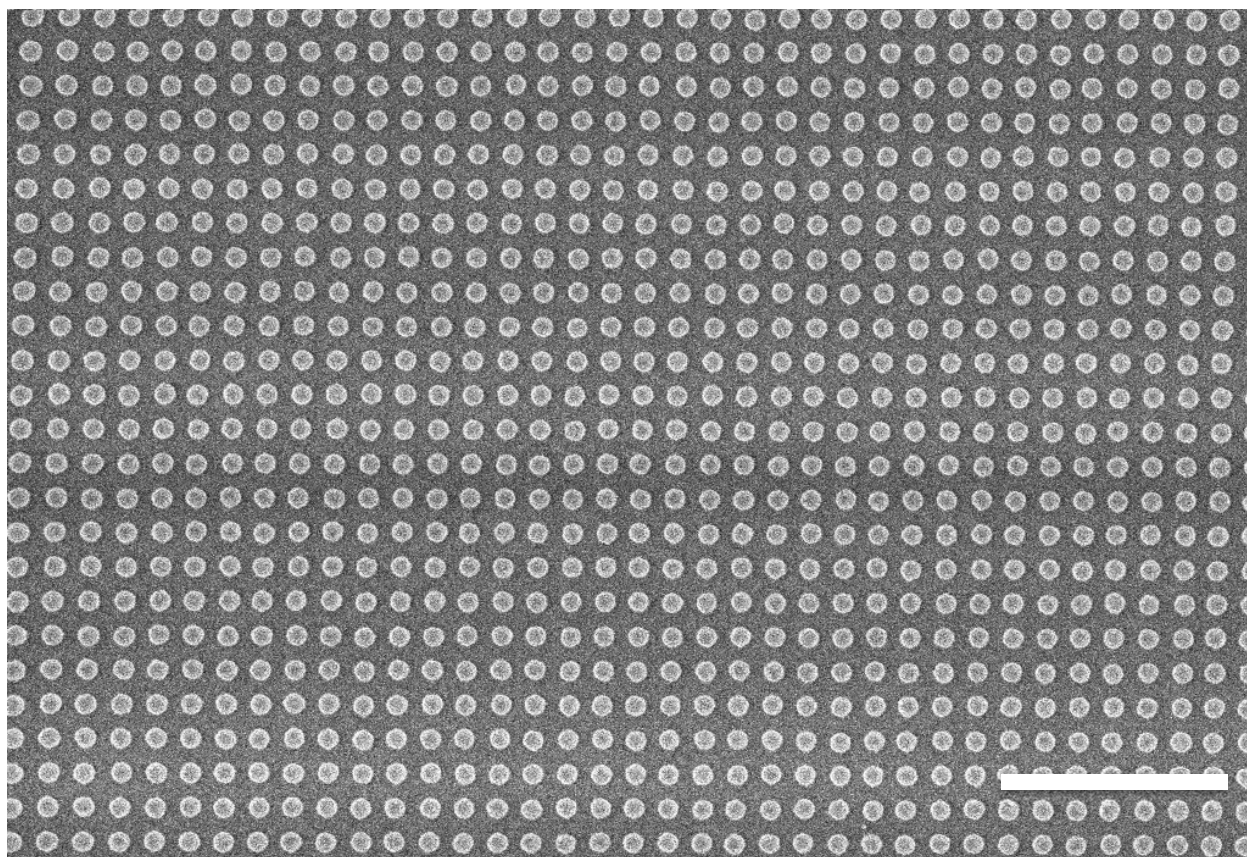


Figure 5.5 SEM image of the fabricated sample. Scalebar represents  $1\mu\text{m}$

Finally, a protective SiN layer is deposited on top of the disk arrays to do spectroscopic characterization. Temperature-dependent characterization of the disk array is performed with a VASE ellipsometer with a modified heating stage (experimental setup identical to [205]).

Figure 5.6 shows the temperature-dependent spectroscopic measurement of the sample. The sample shows a similar trend to the reflection spectra simulated in Figure 5.3, with a much higher reflection peak inside the band. This effect could be due to several contributing factors. Firstly, the

non-conformal deposition of SiN would cause additional reflection and cause the particle. Secondly, the deposition of SiN with LPCVD may cause degradation of the top TiN layer.

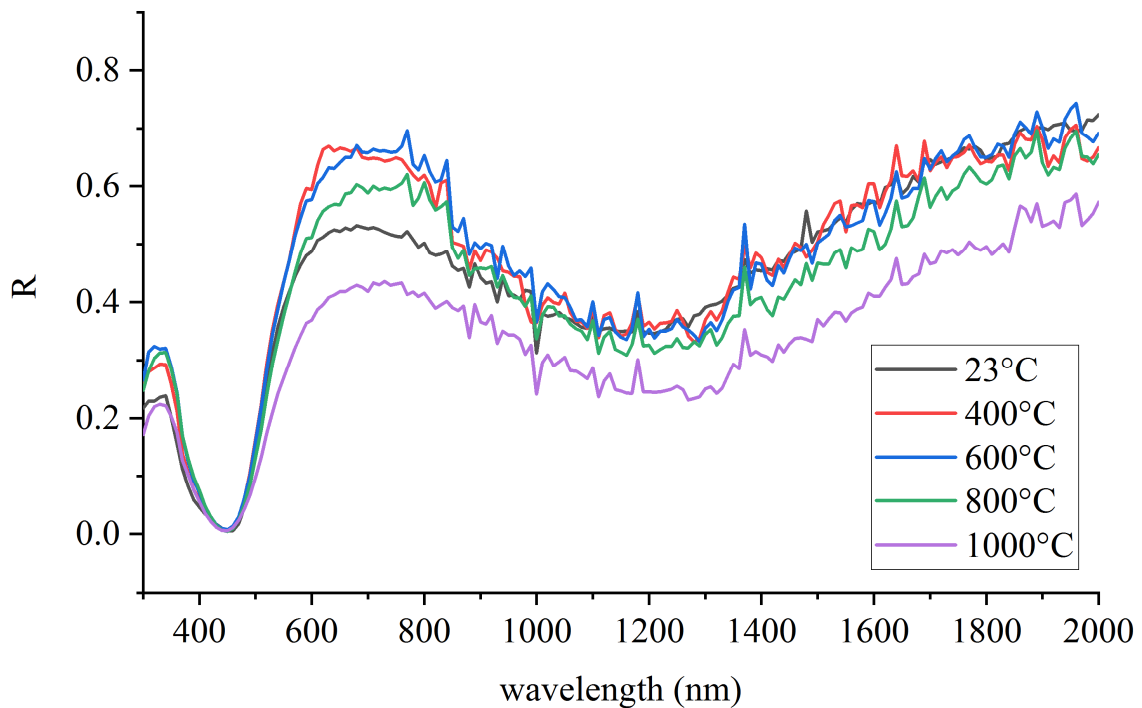


Figure 5.6 Temperature dependent spectroscopic characterization of the TPV sample

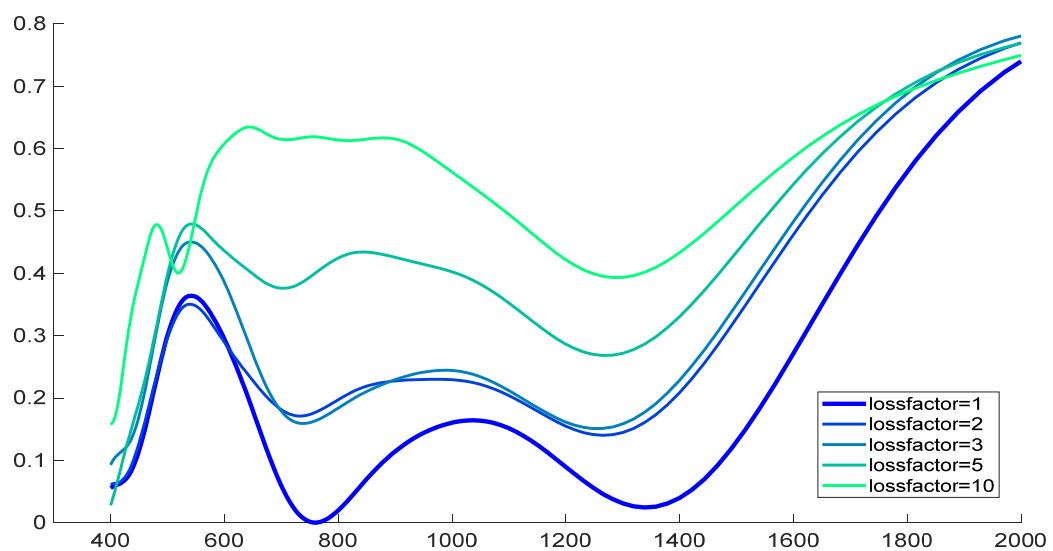


Figure 5.7 Simulation of TPV structure with increased loss in the 30 nm TiN layer

To study the effect, we modify the imaginary part of the 30 nm TiN layer (as shown in Figure 5.3(b) ) by a loss-factor multiplier,  $\epsilon_{r,new} = \epsilon'_r + lossfactor \times i\epsilon''_r$ . Figure 5.7 shows the simulation results for different loss factors at room-temperature. The result indicates that the losses of the top TiN increased significantly, up to a factor of 10.

#### 5.4.4 Large area prototype fabrication

To measure the efficiency of actual thermo-photovoltaic conversion, a system with photo-voltaic cell, heater, and emitters need to be integrated into a tandem. Therefore, the emitter size needs to be comparable to the photovoltaic cell dimension. For practical systems, the e-beam lithography would be too costly and time-consuming to mass manufacture samples. Nano-imprint lithography could be a viable alternative. The nanoimprinting technique can easily replace the e-beam exposure step of prototype fabrication, with all the coating layers deposition steps identical to the prototype. Figure 5.8 shows the possible implementation of large-scale manufacturing of the emitter samples.

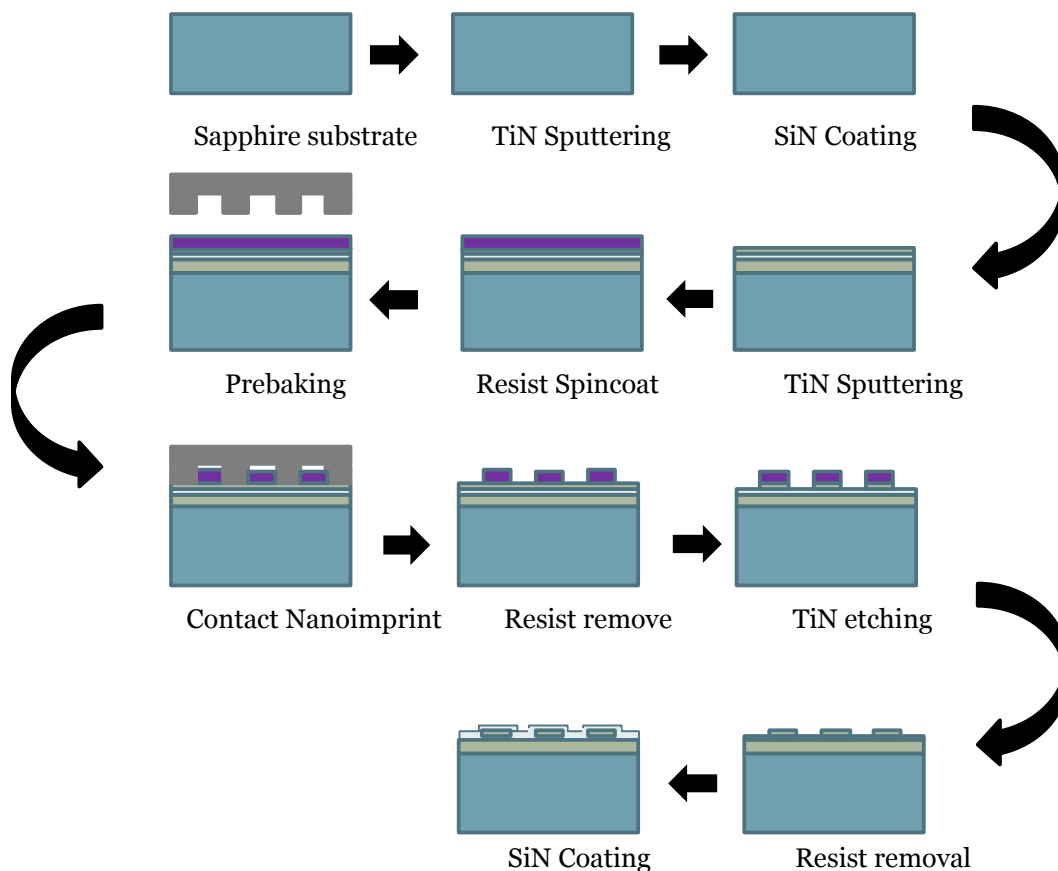


Figure 5.8 Steps for nano-imprint lithography of emitter structures

## **5.5 Concluding Remarks and Roadmap**

The metasurfaces emitter for the thermo-photovoltaic application can improve the efficiency of photovoltaic cells. Fabrication challenges for mass manufacturing need to be addressed for demonstration of the device in large scale. In addition to mitigating the fabrication challenges, the following technological breakthroughs need to be achieved for a metasurface based emitter to be commercially viable. First, TiN needs to be grown at a low temperature while maintaining good plasmonic properties. Second, new etch recipes need to be developed, which can etch refractory materials while retaining the optical properties. Then, CMOS compatible, low loss, dielectric materials that are lattice-matched with the refractory material should be developed to survive high temperatures and should be compatible with a refractory material platform. Finally, new materials should be explored at elevated temperatures for refractory plasmonic applications.

## 6. CONCLUSION

Metasurfaces would continue finding application in new fields and devices. Plasmonic metasurfaces remain a relevant field for the tight confinement of light and device fabrication with a low footprint. The challenge remains to find the balance between plasmonic materials in the visible with the loss but tighter confinement and dielectric materials which have larger feature sizes but extremely low loss. Dielectric metasurfaces offer the a optical loss-free solution, but at the cost of increased device footprint. Emerging material platforms with specialized applications are constantly explored. Material platforms with tunable optical properties, ultra-compact 2D materials, refractory plasmonic materials find their own applications for field confinement, detection and specialized applications. Epitaxially grown monocrystalline silver film can be useful to mitigate the loss and have higher efficiency for plasmonic structures. Color holograms for all the visible spectrum is designed with it. Refractory titanium nitride is used for preparing plasmonic nanoparticles for heating and emitter fabrication. Refractory plasmonic MSs are establishing a field for potential markets where not only high temperatures but harsh environments, in general, need to be tolerated. The applications could go beyond solar and waste heat harvesting and include high temperature and high-power sensors, heat-assisted magnetic recording (HAMR), and photocatalysis – the areas that could potentially benefit from the use of refractory MS optical elements. Unparalleled functional benefits could be offered by refractory metasurfaces equipped with novel plasmonic materials. Their implementation in practical systems and mass production are the next milestones to be achieved.

## REFERENCES

- [1] V. G. Veselago, “The electrodynamics of substances with simultaneously negative values of  $\epsilon$  and  $\mu$ ,” *Sov. Phys. Uspekhi*, vol. 10, no. 4, pp. 509–514, Apr. 1968.
- [2] J. B. Pendry, “Negative Refraction Makes a Perfect Lens,” *Phys. Rev. Lett.*, vol. 85, no. 18, pp. 3966–3969, Oct. 2000.
- [3] R. A. Shelby, D. R. Smith, and S. Schultz, “Experimental verification of a negative index of refraction,” *Science*, vol. 292, no. 5514, pp. 77–9, Apr. 2001.
- [4] D. Schurig, J. J. Mock, B. J. Justice, S. A. Cummer, J. B. Pendry, A. F. Starr, and D. R. Smith, “Metamaterial electromagnetic cloak at microwave frequencies,” *Science*, vol. 314, no. 5801, pp. 977–80, Nov. 2006.
- [5] C. L. Holloway, A. Dienstfrey, E. F. Kuester, J. F. O’Hara, A. K. Azad, and A. J. Taylor, “Characterization of a metafilm/metasurface,” in *2009 IEEE Antennas and Propagation Society International Symposium*, 2009, pp. 1–3.
- [6] N. Yu and F. Capasso, “Flat optics with designer metasurfaces,” *Nat. Mater.*, vol. 13, no. 2, pp. 139–150, 2014.
- [7] D. Cline, *Variational Principles in Classical Mechanics*. 2017.
- [8] N. Yu, P. Genevet, M. A. Kats, F. Aieta, J.-P. Tetienne, F. Capasso, and Z. Gaburro, “Light Propagation with Phase Discontinuities: Generalized Laws of Reflection and Refraction,” *Science*, vol. 334, no. 6054, pp. 333–337, Oct. 2011.
- [9] A. Pors, O. Albrektsen, I. P. Radko, and S. I. Bozhevolnyi, “Gap plasmon-based metasurfaces for total control of reflected light,” vol. 3, p. 2155, Jul. 2013.
- [10] M. Khorasaninejad, W. T. Chen, R. C. Devlin, J. Oh, A. Y. Zhu, and F. Capasso, “Metalenses at visible wavelengths: Diffraction-limited focusing and subwavelength resolution imaging,” *Science*, vol. 352, no. 6290, 2016.
- [11] P. Lalanne, S. Astilean, P. Chavel, E. Cambril, and H. Launois, “Blazed binary subwavelength gratings with efficiencies larger than those of conventional échelette gratings,” *Opt. Lett.*, vol. 23, no. 14, p. 1081, Jul. 1998.

- [12] A. Arbabi, Y. Horie, M. Bagheri, and A. Faraon, “Dielectric metasurfaces for complete control of phase and polarization with subwavelength spatial resolution and high transmission,” *Nat Nano*, vol. 10, no. 11, pp. 937–943, Nov. 2015.
- [13] V. M. Shalaev, W. Cai, U. K. Chettiar, H.-K. Yuan, A. K. Sarychev, V. P. Drachev, and A. V Kildishev, “Negative index of refraction in optical metamaterials.,” *Opt. Lett.*, vol. 30, no. 24, pp. 3356–3358, 2005.
- [14] F. Qin, L. Ding, L. Zhang, F. Monticone, C. C. Chum, J. Deng, S. Mei, Y. Li, J. Teng, M. Hong, S. Zhang, A. Alù, and C.-W. Qiu, “Hybrid bilayer plasmonic metasurface efficiently manipulates visible light,” *Sci. Adv.*, vol. 2, no. 1, 2016.
- [15] J. B. Khurgin and A. Boltasseva, “Reflecting upon the losses in plasmonics and metamaterials,” *MRS Bull.*, vol. 37, no. 08, pp. 768–779, Aug. 2012.
- [16] M. Decker, I. Staude, M. Falkner, J. Dominguez, D. N. Neshev, I. Brener, T. Pertsch, and Y. S. Kivshar, “High-Efficiency Dielectric Huygens’ Surfaces,” *Adv. Opt. Mater.*, vol. 3, no. 6, pp. 813–820, Jun. 2015.
- [17] M. Decker, I. Staude, M. Falkner, J. Dominguez, D. N. Neshev, I. Brener, T. Pertsch, and Y. S. Kivshar, “High-efficiency light-wave control with all-dielectric optical Huygens’ metasurfaces,” *Adv. Opt. Mater.*, vol. 3, no. 6, pp. 813–820, 2014.
- [18] H.-H. Hsiao, C. H. Chu, and D. P. Tsai, “Fundamentals and Applications of Metasurfaces,” *Small Methods*, vol. 1, no. 4, p. 1600064, Apr. 2017.
- [19] S. Pancharatnam, “GENERALIZED THEORY OF INTERFERENCE,” *Reson. J. Sci.*, vol. 18, no. April 2013, pp. 77–78, 2013.
- [20] M. V. Berry, “Quantal Phase Factors Accompanying Adiabatic Changes,” *Proc. R. Soc. A Math. Phys. Eng. Sci.*, vol. 392, no. 1802, pp. 45–57, Mar. 1984.
- [21] M. V. Berry, “The Adiabatic Phase and Pancharatnam’s Phase for Polarized Light,” *J. Mod. Opt.*, vol. 34, no. 11, pp. 1401–1407, Nov. 1987.
- [22] M. V Berry, “Quantal Phase Factors Accompanying Adiabatic Changes,” *Proc. R. Soc. London A Math. Phys. Eng. Sci.*, vol. 392, no. 1802, pp. 45–57, 1984.
- [23] Z. Bomzon, G. Biener, V. Kleiner, and E. Hasman, “Space-variant Pancharatnam–Berry phase optical elements with computer-generated subwavelength gratings,” *Opt. Lett.*, vol. 27, no. 13, p. 1141, Jul. 2002.

- [24] M. Kang, T. Feng, H.-T. Wang, and J. Li, “Wave front engineering from an array of thin aperture antennas,” *Opt. Express*, vol. 20, no. 14, p. 15882, Jul. 2012.
- [25] F. Aieta, P. Genevet, M. A. Kats, N. Yu, R. Blanchard, Z. Gaburro, and F. Capasso, “Aberration-free ultrathin flat lenses and axicons at telecom wavelengths based on plasmonic metasurfaces,” *Nano Lett.*, vol. 12, no. 9, pp. 4932–4936, 2012.
- [26] A. Pors, M. G. Nielsen, R. L. Eriksen, and S. I. Bozhevolnyi, “Broadband focusing flat mirrors based on plasmonic gradient metasurfaces,” *Nano Lett.*, vol. 13, no. 2, pp. 829–834, 2013.
- [27] S. Xiao, F. Zhong, H. Liu, S. Zhu, and J. Li, “Flexible coherent control of plasmonic spin-Hall effect,” *Nat. Commun.*, vol. 6, p. 8360, Sep. 2015.
- [28] J. Lin, J. P. B. Mueller, Q. Wang, G. Yuan, N. Antoniou, X.-C. Yuan, and F. Capasso, “Polarization-Controlled Tunable Directional Coupling of Surface Plasmon Polaritons,” *Science*, vol. 340, no. 6130, pp. 331–334, Apr. 2013.
- [29] M. Khorasaninejad, W. T. Chen, J. Oh, and F. Capasso, “Super-Dispersive Off-Axis Meta-Lenses for Compact High Resolution Spectroscopy,” *Nano Lett.*, vol. 16, no. 2, p. acs.nanolett.6b01097, Jun. 2016.
- [30] A. Shaltout, J. Liu, A. Kildishev, and V. Shalaev, “Photonic spin Hall effect in gap-plasmon metasurfaces for on-chip chiroptical spectroscopy,” *Optica*, vol. 2, no. 10, p. 860, Oct. 2015.
- [31] Y. Zhao and A. Alù, “Manipulating light polarization with ultrathin plasmonic metasurfaces,” *Phys. Rev. B*, vol. 84, no. 20, p. 205428, Nov. 2011.
- [32] N. Meinzer, W. L. Barnes, and I. R. Hooper, “Plasmonic meta-atoms and metasurfaces,” *Nat. Photonics*, vol. 8, no. 12, pp. 889–898, Nov. 2014.
- [33] S. M. Choudhury, D. Wang, K. Chaudhuri, C. DeVault, A. V. Kildishev, A. Boltasseva, and V. M. Shalaev, “Material platforms for optical metasurfaces,” *Nanophotonics*, vol. 7, no. 6, pp. 959–987, Jun. 2018.
- [34] C. L. Holloway, E. F. Kuester, J. A. Gordon, J. O’Hara, J. Booth, and D. R. Smith, “An Overview of the Theory and Applications of Metasurfaces: The Two-Dimensional Equivalents of Metamaterials,” *IEEE Antennas Propag. Mag.*, vol. 54, no. 2, pp. 10–35, Apr. 2012.

- [35] A. V. Kildishev, A. Boltasseva, and V. M. Shalaev, "Planar photonics with metasurfaces.," *Science*, vol. 339, no. 6125, p. 1232009, Mar. 2013.
- [36] Nanfang Yu, P. Genevet, F. Aieta, M. A. Kats, R. Blanchard, G. Aoust, J.-P. Tetienne, Z. Gaburro, and F. Capasso, "Flat Optics: Controlling Wavefronts With Optical Antenna Metasurfaces," *IEEE J. Sel. Top. Quantum Electron.*, vol. 19, no. 3, pp. 4700423–4700423, May 2013.
- [37] S. Walia, C. M. Shah, P. Gutruf, H. Nili, D. R. Chowdhury, W. Withayachumnankul, M. Bhaskaran, and S. Sriram, "Flexible metasurfaces and metamaterials: A review of materials and fabrication processes at micro- and nano-scales," *Appl. Phys. Rev.*, vol. 2, no. 1, p. 011303, Mar. 2015.
- [38] A. E. Minovich, A. E. Miroschnichenko, A. Y. Bykov, T. V. Murzina, D. N. Neshev, and Y. S. Kivshar, "Functional and nonlinear optical metasurfaces," *Laser Photon. Rev.*, vol. 9, no. 2, pp. 195–213, Mar. 2015.
- [39] P. Genevet and F. Capasso, "Holographic optical metasurfaces: a review of current progress," *Reports Prog. Phys.*, vol. 78, no. 2, p. 024401, Feb. 2015.
- [40] H.-T. Chen, A. J. Taylor, and N. Yu, "A review of metasurfaces: physics and applications," *Reports Prog. Phys.*, vol. 79, no. 7, p. 076401, Jul. 2016.
- [41] S. B. Glybovski, S. A. Tretyakov, P. A. Belov, Y. S. Kivshar, and C. R. Simovski, "Metasurfaces: From microwaves to visible," *Physics Reports*, vol. 634. North-Holland, pp. 1–72, 24-May-2016.
- [42] A. Y. Zhu, A. I. Kuznetsov, B. Luk'yanchuk, N. Engheta, and P. Genevet, "Traditional and emerging materials for optical metasurfaces," *Nanophotonics*, vol. 6, no. 2, pp. 452–471, Jan. 2017.
- [43] P. Colomban, "The Use of Metal Nanoparticles to Produce Yellow, Red and Iridescent Colour, from Bronze Age to Present Times in Lustre Pottery and Glass: Solid State Chemistry, Spectroscopy and Nanostructure," *J. Nano Res.*, vol. 8, pp. 109–132, Sep. 2009.
- [44] P. Colomban and C. Truong, "Non-destructive Raman study of the glazing technique in lustre potteries and faience(9–14th centuries): silver ions, nanoclusters, microstructure and processing," *J. Raman Spectrosc.*, vol. 35, no. 3, pp. 195–207, Mar. 2004.

- [45] L. B. Hunt, “Gold based glass and enamel colours,” *Endeavour*, vol. 5, no. 2, pp. 61–67, Jan. 1981.
- [46] X. Yin, Z. Ye, J. Rho, Y. Wang, and X. Zhang, “Photonic Spin Hall Effect at Metasurfaces,” *Science*, vol. 339, no. 6126, pp. 1405–1407, Mar. 2013.
- [47] M. W. Knight, L. Liu, Y. Wang, L. Brown, S. Mukherjee, N. S. King, H. O. Everitt, P. Nordlander, and N. J. Halas, “Aluminum Plasmonic Nanoantennas,” *Nano Lett.*, vol. 12, no. 11, pp. 6000–6004, Nov. 2012.
- [48] T. Xu, C. Du, C. Wang, and X. Luo, “Subwavelength imaging by metallic slab lens with nanoslits,” *Appl. Phys. Lett.*, vol. 91, no. 20, p. 201501, Nov. 2007.
- [49] W. Srituravanich, L. Pan, Y. Wang, C. Sun, D. B. Bogy, and X. Zhang, “Flying plasmonic lens in the near field for high-speed nanolithography,” *Nat. Nanotechnol.*, vol. 3, no. 12, pp. 733–737, Dec. 2008.
- [50] X. Ni, S. Ishii, A. V Kildishev, and V. M. Shalaev, “Ultra-thin, planar, Babinet-inverted plasmonic metalenses,” *Light Sci. Appl.*, vol. 2, no. 4, p. e72, Apr. 2013.
- [51] X. Chen, L. Huang, H. Mühlenbernd, G. Li, B. Bai, Q. Tan, G. Jin, C.-W. Qiu, S. Zhang, and T. Zentgraf, “Dual-polarity plasmonic metalens for visible light,” *Nat. Commun.*, vol. 3, p. 1198, Nov. 2012.
- [52] Z. Li, E. Palacios, S. Butun, and K. Aydin, “Visible-Frequency Metasurfaces for Broadband Anomalous Reflection and High-Efficiency Spectrum Splitting,” *Nano Lett.*, vol. 15, no. 3, pp. 1615–1621, Mar. 2015.
- [53] X. Ni, A. V Kildishev, and V. M. Shalaev, “Metasurface holograms for visible light,” *Nat. Commun.*, vol. 4, p. 2807, 2013.
- [54] F. Zhou, Y. Liu, and W. Cai, “Plasmonic holographic imaging with V-shaped nanoantenna array,” *Opt. Express*, vol. 21, no. 4, p. 4348, Feb. 2013.
- [55] Y. Montelongo, J. O. Tenorio-Pearl, W. I. Milne, and T. D. Wilkinson, “Polarization Switchable Diffraction Based on Subwavelength Plasmonic Nanoantennas,” *Nano Lett.*, vol. 14, no. 1, pp. 294–298, Jan. 2014.
- [56] L. Huang, X. Chen, H. Mühlenbernd, H. Zhang, S. Chen, B. Bai, Q. Tan, G. Jin, K.-W. Cheah, C.-W. Qiu, J. Li, T. Zentgraf, and S. Zhang, “Three-dimensional optical holography using a plasmonic metasurface,” *Nat. Commun.*, vol. 4, no. May, p. 2808, 2013.

- [57] G. Zheng, H. Mühlenbernd, M. Kenney, G. Li, T. Zentgraf, and S. Zhang, “Metasurface holograms reaching 80% efficiency,” *Nat. Nanotechnol.*, vol. 10, no. 4, pp. 308–312, Feb. 2015.
- [58] D. Wen, F. Yue, G. Li, G. Zheng, K. Chan, S. Chen, M. Chen, K. F. Li, P. W. H. Wong, K. W. Cheah, E. Yue Bun Pun, S. Zhang, and X. Chen, “Helicity multiplexed broadband metasurface holograms,” *Nat. Commun.*, vol. 6, p. 8241, Sep. 2015.
- [59] W. T. Chen, K.-Y. Y. Yang, C.-M. M. Wang, Y.-W. W. Huang, G. Sun, I.-D. Da Chiang, C. Y. Liao, W.-L. L. Hsu, H. T. Lin, S. Sun, L. Zhou, A. Q. Liu, and D. P. Tsai, “High-efficiency broadband meta-hologram with polarization-controlled dual images,” *Nano Lett.*, vol. 14, no. 1, pp. 225–230, Jan. 2014.
- [60] W. Ye, F. Zeuner, X. Li, B. Reineke, S. He, C.-W. Qiu, J. Liu, Y. Wang, S. Zhang, and T. Zentgraf, “Spin and wavelength multiplexed nonlinear metasurface holography,” *Nat. Commun.*, vol. 7, p. 11930, Jun. 2016.
- [61] Y. Montelongo, J. O. Tenorio-Pearl, C. Williams, S. Zhang, W. I. Milne, and T. D. Wilkinson, “Plasmonic nanoparticle scattering for color holograms,” *Proc. Natl. Acad. Sci. U. S. A.*, vol. 111, no. 7, pp. 1–5, Sep. 2014.
- [62] Y.-W. W. Huang, W. T. Chen, W.-Y. Y. Tsai, P. C. Wu, C.-M. M. Wang, G. Sun, and D. P. Tsai, “Aluminum plasmonic multicolor meta-Hologram,” *Nano Lett.*, vol. 15, no. 5, pp. 3122–3127, May 2015.
- [63] X. Li, L. Chen, Y. Li, X. Zhang, M. Pu, Z. Zhao, X. Ma, Y. Wang, M. Hong, and X. Luo, “Multicolor 3D meta-holography by broadband plasmonic modulation,” *Sci. Adv.*, vol. 2, no. 11, pp. e1601102–e1601102, Nov. 2016.
- [64] S. Choudhury, U. Guler, A. Shaltout, V. M. Shalaev, A. V. Kildishev, and A. Boltasseva, “Pancharatnam-Berry Phase Manipulating Metasurface for Visible Color Hologram Based on Low Loss Silver Thin Film,” *Adv. Opt. Mater.*, vol. 5, no. 10, p. 1700196, May 2017.
- [65] N. Yu, F. Aieta, P. Genevet, M. A. Kats, Z. Gaburro, and F. Capasso, “A Broadband, Background-Free Quarter-Wave Plate Based on Plasmonic Metasurfaces,” *Nano Lett.*, vol. 12, no. 12, pp. 6328–6333, Dec. 2012.
- [66] E. Karimi, S. A. Schulz, I. De Leon, H. Qassim, J. Upham, and R. W. Boyd, “Generating optical orbital angular momentum at visible wavelengths using a plasmonic metasurface,” *Light Sci. Appl.*, vol. 3, no. 5, p. e167, May 2014.

- [67] F. Ding, Z. Wang, S. He, V. M. Shalaev, and A. V. Kildishev, "Broadband high-efficiency half-wave plate: A supercell-based plasmonic metasurface approach," *ACS Nano*, vol. 9, no. 4, pp. 4111–4119, 2015.
- [68] A. Pors and S. I. Bozhevolnyi, "Efficient and broadband quarter-wave plates by gap-plasmon resonators," *Opt. Express*, vol. 21, no. 3, p. 2942, Feb. 2013.
- [69] F. Yue, D. Wen, J. Xin, B. D. Gerardot, J. Li, and X. Chen, "Vector Vortex Beam Generation with a Single Plasmonic Metasurface," *ACS Photonics*, vol. 3, no. 9, pp. 1558–1563, 2016.
- [70] W. Wang, Y. Li, Z. Guo, R. Li, J. Zhang, A. Zhang, and S. Qu, "Ultra-thin optical vortex phase plate based on the metasurface and the angular momentum transformation," *J. Opt.*, vol. 17, no. 4, p. 045102, Apr. 2015.
- [71] P. Genevet, N. Yu, F. Aieta, J. Lin, M. A. Kats, R. Blanchard, M. O. Scully, Z. Gaburro, and F. Capasso, "Ultra-thin plasmonic optical vortex plate based on phase discontinuities," *Appl. Phys. Lett.*, vol. 100, no. 1, p. 013101, Jan. 2012.
- [72] X. Ni, Z. J. Z. J. Wong, M. Mrejen, Y. Wang, and X. Zhang, "An ultrathin invisibility skin cloak for visible light," *Science*, vol. 349, no. 6254, pp. 1310–1314, Sep. 2015.
- [73] J. Kim, S. Choudhury, C. DeVault, Y. Zhao, A. V. Kildishev, V. M. Shalaev, A. Alù, A. Boltasseva, A. Al??, and A. Boltasseva, "Controlling the Polarization State of Light with Plasmonic Metal Oxide Metasurface," *ACS Nano*, vol. 10, no. 10, pp. 9326–9333, Oct. 2016.
- [74] S. Ishii, A. V Kildishev, V. M. Shalaev, K.-P. Chen, and V. P. Drachev, "Metal nanoslit lenses with polarization-selective design.," *Opt. Lett.*, vol. 36, no. 4, pp. 451–3, 2011.
- [75] Y. Yang, W. Wang, P. Moitra, I. I. Kravchenko, D. P. Briggs, and J. Valentine, "Dielectric meta-reflectarray for broadband linear polarization conversion and optical vortex generation," *Nano Lett.*, vol. 14, no. 3, pp. 1394–1399, 2014.
- [76] J. B. Khurgin, "How to deal with the loss in plasmonics and metamaterials," *Nat Nano*, vol. 10, no. 1, pp. 2–6, Jan. 2015.
- [77] V. S. Asadchy, A. Wickberg, A. Díaz-Rubio, and M. Wegener, "Eliminating Scattering Loss in Anomalously Reflecting Optical Metasurfaces," *ACS Photonics*, vol. 4, no. 5, pp. 1264–1270, May 2017.

- [78] S. Yokogawa, S. P. Burgos, and H. A. Atwater, "Plasmonic Color Filters for CMOS Image Sensor Applications," *Nano Lett.*, vol. 12, no. 8, pp. 4349–4354, Aug. 2012.
- [79] J. S. Clausen, E. Højlund-Nielsen, A. B. Christiansen, S. Yazdi, M. Grajower, H. Taha, U. Levy, A. Kristensen, and N. A. Mortensen, "Plasmonic Metasurfaces for Coloration of Plastic Consumer Products," *Nano Lett.*, vol. 14, no. 8, pp. 4499–4504, Aug. 2014.
- [80] A. S. Roberts, A. Pors, O. Albrektsen, and S. I. Bozhevolnyi, "Subwavelength Plasmonic Color Printing Protected for Ambient Use," *Nano Lett.*, vol. 14, no. 2, pp. 783–787, Feb. 2014.
- [81] S. Kruk, M. Weismann, A. Y. Bykov, E. A. Mamonov, I. A. Kolmychek, T. Murzina, N. C. Panoiu, D. N. Neshev, and Y. S. Kivshar, "Enhanced Magnetic Second-Harmonic Generation from Resonant Metasurfaces," *ACS Photonics*, vol. 2, no. 8, pp. 1007–1012, Aug. 2015.
- [82] E. A. Mamonov, I. A. Kolmychek, A. I. Maydykovsky, and T. V. Murzina, "Second Harmonic Generation in Planar Chiral Nanostructures," *Bull. Russ. Acad. Sci.*, vol. 77, no. 1, pp. 66–68, Jan. 2013.
- [83] R. Chandrasekar, N. K. Emani, A. Lagutchev, V. M. Shalaev, C. Ciraci, D. R. Smith, and A. V. Kildishev, "Second harmonic generation with plasmonic metasurfaces: direct comparison of electric and magnetic resonances," *Opt. Mater. Express*, vol. 5, no. 11, p. 2682, Nov. 2015.
- [84] J. S. Gomez-Diaz, J. Lee, M. Tymchenko, M. A. Belkin, A. Alù, and A. Alu, "Giant nonlinear processes in plasmonic metasurfaces," in *2015 IEEE International Symposium on Antennas and Propagation & USNC/URSI National Radio Science Meeting*, 2015, vol. 2015–Octob, pp. 1084–1085.
- [85] M. Tymchenko, J. S. Gomez-Diaz, J. Lee, N. Nookala, M. A. Belkin, and A. Alù, "Gradient Nonlinear Pancharatnam-Berry Metasurfaces," *Phys. Rev. Lett.*, vol. 115, no. 20, p. 207403, Nov. 2015.
- [86] E. Panchenko, J. J. Cadusch, T. D. James, and A. Roberts, "Plasmonic Metasurface-Enabled Differential Photodetectors for Broadband Optical Polarization Characterization," *ACS Photonics*, vol. 3, no. 10, pp. 1833–1839, Oct. 2016.

- [87] J. Fang, D. Wang, C. T. DeVault, T.-F. Chung, Y. P. Chen, A. Boltasseva, V. M. Shalaev, and A. V. Kildishev, “Enhanced Graphene Photodetector with Fractal Metasurface,” *Nano Lett.*, vol. 17, no. 1, pp. 57–62, Jan. 2017.
- [88] I. S. Maksymov, “Magneto-plasmonic nanoantennas: Basics and applications,” *Rev. Phys.*, vol. 1, pp. 36–51, Nov. 2016.
- [89] T. S. Luk, S. Campione, I. Kim, S. Feng, Y. C. Jun, S. Liu, J. B. Wright, I. Brener, P. B. Catrysse, S. Fan, and M. B. Sinclair, “Directional perfect absorption using deep subwavelength low-permittivity films,” *Phys. Rev. B - Condens. Matter Mater. Phys.*, vol. 90, no. 8, pp. 1–10, Aug. 2014.
- [90] F. Ding, J. Dai, Y. Chen, J. Zhu, Y. Jin, and S. I. Bozhevolnyi, “Broadband near-infrared metamaterial absorbers utilizing highly lossy metals,” *Sci. Rep.*, vol. 6, no. 1, p. 39445, Dec. 2016.
- [91] K. Aydin, V. E. Ferry, R. M. Briggs, and H. A. Atwater, “Broadband polarization-independent resonant light absorption using ultrathin plasmonic super absorbers,” *Nat. Commun.*, vol. 2, p. 517, Nov. 2011.
- [92] Z. H. Jiang, S. Yun, F. Toor, D. H. Werner, and T. S. Mayer, “Conformal Dual-Band Near-Perfectly Absorbing Mid-Infrared Metamaterial Coating,” *ACS Nano*, vol. 5, no. 6, pp. 4641–4647, Jun. 2011.
- [93] C. Argyropoulos, K. Q. Le, N. Mattiucci, G. D’Aguanno, and A. Alù, “Broadband absorbers and selective emitters based on plasmonic Brewster metasurfaces,” *Phys. Rev. B*, vol. 87, no. 20, p. 205112, May 2013.
- [94] G. M. Akselrod, J. Huang, T. B. Hoang, P. T. Bowen, L. Su, D. R. Smith, and M. H. Mikkelsen, “Large-Area Metasurface Perfect Absorbers from Visible to Near-Infrared,” *Adv. Mater.*, vol. 27, no. 48, pp. 8028–8034, Dec. 2015.
- [95] C. Ng, J. J. Cadusch, S. Dligatch, A. Roberts, T. J. Davis, P. Mulvaney, and D. E. Gómez, “Hot Carrier Extraction with Plasmonic Broadband Absorbers,” *ACS Nano*, vol. 10, no. 4, pp. 4704–4711, Apr. 2016.
- [96] U. Guler, a. Boltasseva, and V. M. Shalaev, “Refractory Plasmonics,” *Science*, vol. 344, no. 6181, pp. 263–264, 2014.

- [97] J. A. Dionne, A. Baldi, B. Baum, C.-S. Ho, V. Janković, G. V. Naik, T. Narayan, J. A. Scholl, and Y. Zhao, “Localized fields, global impact: Industrial applications of resonant plasmonic materials,” *MRS Bull.*, vol. 40, no. 12, pp. 1138–1145, Dec. 2015.
- [98] P. R. West, S. Ishii, G. V. Naik, N. K. Emani, V. M. Shalaev, and A. Boltasseva, “Searching for better plasmonic materials,” *Laser Photonics Rev.*, vol. 4, no. 6, pp. 795–808, Nov. 2010.
- [99] P. Genevet, F. Capasso, F. Aieta, M. Khorasaninejad, and R. Devlin, “Recent advances in planar optics: from plasmonic to dielectric metasurfaces,” *Optica*, vol. 4, no. 1, p. 139, Jan. 2017.
- [100] I. Staude and J. Schilling, “Metamaterial-inspired silicon nanophotonics,” *Nat. Photonics*, vol. 11, no. 5, pp. 274–284, Apr. 2017.
- [101] S. Jahani and Z. Jacob, “All-dielectric metamaterials,” *Nat. Nanotechnol.*, vol. 11, no. 1, pp. 23–36, Jan. 2016.
- [102] A. I. Kuznetsov, A. E. Miroshnichenko, M. L. Brongersma, Y. S. Kivshar, and B. Luk’yanchuk, “Optically resonant dielectric nanostructures,” *Science*, vol. 354, no. 6314, 2016.
- [103] S. Campione, S. Liu, L. I. Basilio, L. K. Warne, W. L. Langston, T. S. Luk, J. R. Wendt, J. L. Reno, G. A. Keeler, I. Brener, and M. B. Sinclair, “Broken Symmetry Dielectric Resonators for High Quality Factor Fano Metasurfaces,” *ACS Photonics*, vol. 3, no. 12, pp. 2362–2367, Dec. 2016.
- [104] Y. Yang, I. I. Kravchenko, D. P. Briggs, and J. Valentine, “All-dielectric metasurface analogue of electromagnetically induced transparency,” *Nat. Commun.*, vol. 5, p. 5753, Dec. 2014.
- [105] M. Kerker, D.-S. Wang, and C. L. Giles, “Electromagnetic scattering by magnetic spheres,” *J. Opt. Soc. Am.*, vol. 73, no. 6, p. 765, Jun. 1983.
- [106] W. Li, U. Guler, N. Kinsey, G. V. Naik, A. A. Boltasseva, J. Guan, V. M. Shalaev, and A. V. A. V. Kildishev, “Refractory plasmonics with titanium nitride: Broadband,” *Adv. Mater.*, vol. 26, no. 47, pp. 7959–7965, Dec. 2014.
- [107] U. Guler, J. C. Ndukaife, G. V. Naik, A. G. A. Nnanna, A. V. Kildishev, V. M. Shalaev, and A. Boltasseva, “Local heating with lithographically fabricated plasmonic titanium nitride nanoparticles,” *Nano Lett.*, vol. 13, no. 12, pp. 6078–6083, Dec. 2013.

- [108] K. Chaudhuri, A. Shaltout, U. Guler, V. M. Shalaev, and A. Boltasseva, “High efficiency phase gradient metasurface using refractory plasmonic Zirconium Nitride,” in *Conference on Lasers and Electro-Optics*, 2016, p. FM3N.2.
- [109] K. Reichelt and H. Lutz, “Hetero-epitaxial growth of vacuum evaporated silver and gold,” *J. Cryst. Growth*, vol. 10, no. 1, pp. 103–107, Jun. 1971.
- [110] H. Bialas and K. Heneka, “Epitaxy of fcc metals on dielectric substrates,” *Vacuum*, vol. 45, no. 1, pp. 79–87, Jan. 1994.
- [111] Y. Gotoh and S. Ino, “Epitaxial growth of silver on an Si(111)  $7\times 7$  surface at room temperature,” *Thin Solid Films*, vol. 109, no. 3, pp. 255–261, Nov. 1983.
- [112] D. Gu, C. Zhang, Y.-K. Wu, and L. J. Guo, “Ultrasoother and Thermally Stable Silver-Based Thin Films with Subnanometer Roughness by Aluminum Doping,” *ACS Nano*, vol. 8, no. 10, pp. 10343–10351, Oct. 2014.
- [113] G. Beck, C. Bachmann, R. Bretzler, and R. Kmeth, “Epitaxial and non-epitaxial platinum, palladium and silver films on yttrium-stabilised zirconia,” *Mater. Chem. Phys.*, vol. 158, pp. 107–114, May 2015.
- [114] A. A. High, R. C. Devlin, A. Dibos, M. Polking, D. S. Wild, J. Perczel, N. P. De Leon, M. D. Lukin, and H. Park, “Visible-frequency hyperbolic metasurface,” *Nature*, vol. 522, no. 7555, pp. 192–196, Jun. 2015.
- [115] M. I. Shalaev, J. Sun, A. Tsukernik, A. Pandey, K. Nikolskiy, and N. M. Litchinitser, “High-Efficiency All-Dielectric Metasurfaces for Ultracompact Beam Manipulation in Transmission Mode,” *Nano Lett.*, vol. 15, no. 9, pp. 6261–6266, Sep. 2015.
- [116] P. Moitra, B. A. Slovick, Z. Gang Yu, S. Krishnamurthy, and J. Valentine, “Experimental demonstration of a broadband all-dielectric metamaterial perfect reflector,” *Appl. Phys. Lett.*, vol. 104, no. 17, p. 171102, Apr. 2014.
- [117] P. R. West, J. L. Stewart, A. V. Kildishev, V. M. Shalaev, V. V. Shkunov, F. Strohkendl, Y. A. Zakharenkov, R. K. Dodds, and R. Byren, “All-dielectric subwavelength metasurface focusing lens,” *Opt. Express*, vol. 22, no. 21, p. 26212, Oct. 2014.
- [118] S. W. Kim, K. J. Yee, M. Abashin, L. Pang, and Y. Fainman, “Composite dielectric metasurfaces for phase control of vector field,” *Opt. Lett.*, vol. 40, no. 11, p. 2453, Jun. 2015.

- [119] M. Khorasaninejad, A. Ambrosio, P. Kanhaiya, and F. Capasso, “Broadband and chiral binary dielectric meta-holograms,” *Sci. Adv.*, vol. 2, no. 5, pp. e1501258–e1501258, May 2016.
- [120] D. Ohana, B. Desiatov, N. Mazurski, and U. Levy, “Dielectric Metasurface as a Platform for Spatial Mode Conversion in Nanoscale Waveguides,” *Nano Lett.*, vol. 16, no. 12, pp. 7956–7961, 2016.
- [121] Z. Li, M.-H. Kim, C. Wang, Z. Han, S. Shrestha, A. C. Overvig, M. Lu, A. Stein, A. M. Agarwal, M. Lončar, and N. Yu, “Controlling propagation and coupling of waveguide modes using phase-gradient metasurfaces,” *Nat. Nanotechnol.*, vol. 12, no. 7, pp. 675–683, Jul. 2017.
- [122] C.-S. Park, V. R. Shrestha, W. Yue, S. Gao, S.-S. Lee, E.-S. Kim, and D.-Y. Choi, “Structural Color Filters Enabled by a Dielectric Metasurface Incorporating Hydrogenated Amorphous Silicon Nanodisks,” *Sci. Rep.*, vol. 7, no. 1, p. 2556, Dec. 2017.
- [123] A. Zhan, S. Colburn, R. Trivedi, T. K. Fryett, C. M. Dodson, and A. Majumdar, “Low-Contrast Dielectric Metasurface Optics,” *ACS Photonics*, vol. 3, no. 2, pp. 209–214, Feb. 2016.
- [124] P. Lalanne, S. Astilean, P. Chavel, E. Cambрил, and H. Launois, “Design and fabrication of blazed binary diffractive elements with sampling periods smaller than the structural cutoff,” *J. Opt. Soc. Am. A*, vol. 16, no. 5, p. 1143, May 1999.
- [125] P. Lalanne, “Waveguiding in blazed-binary diffractive elements,” *J. Opt. Soc. Am. A*, vol. 16, no. 10, p. 2517, Oct. 1999.
- [126] W. T. Chen, A. Y. Zhu, M. Khorasaninejad, Z. Shi, V. Sanjeev, and F. Capasso, “Immersion Meta-Lenses at Visible Wavelengths for Nanoscale Imaging,” *Nano Lett.*, vol. 17, no. 5, pp. 3188–3194, May 2017.
- [127] M. Khorasaninejad, A. Y. Zhu, C. Roques-Carmes, W. T. Chen, J. Oh, I. Mishra, R. C. Devlin, and F. Capasso, “Polarization-Insensitive Metalenses at Visible Wavelengths,” *Nano Lett.*, vol. 16, no. 11, pp. 7229–7234, Nov. 2016.
- [128] J. P. Balthasar Mueller, N. A. Rubin, R. C. Devlin, B. Groever, and F. Capasso, “Metasurface Polarization Optics: Independent Phase Control of Arbitrary Orthogonal States of Polarization,” *Phys. Rev. Lett.*, vol. 118, no. 11, p. 113901, Mar. 2017.

- [129] A. Y. Zhu, W.-T. Chen, M. Khorasaninejad, J. Oh, A. Zaidi, I. Mishra, R. C. Devlin, and F. Capasso, "Ultra-compact visible chiral spectrometer with meta-lenses," *APL Photonics*, vol. 2, no. 3, p. 036103, Mar. 2017.
- [130] M. Khorasaninejad, W. T. Chen, A. Y. Zhu, J. Oh, R. C. Devlin, D. Rousso, and F. Capasso, "Multispectral Chiral Imaging with a Metalens," *Nano Lett.*, vol. 16, no. 7, pp. 4595–4600, Jul. 2016.
- [131] R. C. Devlin, A. Ambrosio, D. Wintz, S. L. Oscurato, A. Y. Zhu, M. Khorasaninejad, J. Oh, P. Maddalena, and F. Capasso, "Spin-to-orbital angular momentum conversion in dielectric metasurfaces," *Opt. Express*, vol. 25, no. 1, p. 377, Jan. 2017.
- [132] P. Gutruf, C. Zou, W. Withayachumnankul, M. Bhaskaran, S. Sriram, and C. Fumeaux, "Mechanically Tunable Dielectric Resonator Metasurfaces at Visible Frequencies," *ACS Nano*, vol. 10, no. 1, pp. 133–141, Jan. 2016.
- [133] S. Sun, Z. Zhou, C. Zhang, Y. Gao, Z. Duan, S. Xiao, and Q. Song, "All-Dielectric Full-Color Printing with TiO<sub>2</sub> Metasurfaces," *ACS Nano*, vol. 11, no. 5, pp. 4445–4452, May 2017.
- [134] S. Shrestha, Y. Wang, A. C. Overvig, M. Lu, A. Stein, L. D. Negro, and N. Yu, "Indium Tin Oxide Broadband Metasurface Absorber," *ACS Photonics*, vol. 5, no. 9, pp. 3526–3533, Sep. 2018.
- [135] D. C. Adams, S. Inampudi, T. Ribaud, D. Slocum, S. Vangala, N. A. Kuhta, W. D. Goodhue, V. A. Podolskiy, and D. Wasserman, "Funneling Light through a Subwavelength Aperture with Epsilon-Near-Zero Materials," *Phys. Rev. Lett.*, vol. 107, no. 13, p. 133901, Sep. 2011.
- [136] G. V. Naik, V. M. Shalaev, A. Boltasseva, R. V. Gururaj Naik, V. M. Shalaev, A. Boltasseva, G. V. Naik, V. M. Shalaev, and A. Boltasseva, "Alternative Plasmonic Materials: Beyond Gold and Silver," *Adv. Mater.*, vol. 25, no. 24, pp. 3264–3294, Jun. 2013.
- [137] T. R. Gordon, T. Paik, D. R. Klein, G. V. Naik, H. Caglayan, A. Boltasseva, and C. B. Murray, "Shape-Dependent Plasmonic Response and Directed Self-Assembly in a New Semiconductor Building Block, Indium-Doped Cadmium Oxide (ICO)," *Nano Lett.*, vol. 13, no. 6, pp. 2857–2863, Jun. 2013.

- [138] L. Wang, C. Clavero, K. Yang, E. Radue, M. T. Simons, I. Novikova, and R. A. Lukaszew, “Bulk and surface plasmon polariton excitation in RuO<sub>2</sub> for low-loss plasmonic applications in NIR,” *Opt. Express*, vol. 20, no. 8, p. 8618, Apr. 2012.
- [139] M. Abb, P. Albella, J. Aizpurua, and O. L. Muskens, “All-optical control of a single plasmonic nanoantenna-ITO hybrid,” *Nano Lett.*, vol. 11, no. 6, pp. 2457–2463, 2011.
- [140] P. Guo, R. D. Schaller, L. E. Ocola, B. T. Diroll, J. B. Ketterson, and R. P. H. Chang, “Large optical nonlinearity of ITO nanorods for sub-picosecond all-optical modulation of the full-visible spectrum,” *Nat. Commun.*, vol. 7, p. 12892, 2016.
- [141] X. Liu, J.-H. Kang, H. Yuan, J. Park, S. J. Kim, Y. Cui, H. Y. Hwang, and M. L. Brongersma, “Electrical tuning of a quantum plasmonic resonance,” Jun. 2017.
- [142] V. W. Brar, M. S. Jang, M. Sherrott, J. J. Lopez, and H. A. Atwater, “Highly Confined Tunable Mid-Infrared Plasmonics in Graphene Nanoresonators,” *Nano Lett.*, vol. 13, no. 6, pp. 2541–2547, Jun. 2013.
- [143] N. K. Emani, D. Wang, T.-F. Chung, L. J. Prokopenko, A. V. Kildishev, V. M. Shalaev, Y. P. Chen, and A. Boltasseva, “Plasmon resonance in multilayer graphene nanoribbons,” *Laser Photon. Rev.*, vol. 9, no. 6, pp. 650–655, Nov. 2015.
- [144] Q. Ren, J. W. You, and N. C. Panoiu, “Enhanced optical nonlinearity of metasurfaces made of patterned graphene nanoribbons,” in *Advanced Photonics 2018 (BGPP, IPR, NP, NOMA, Sensors, Networks, SPPCom, SOF)*, 2018, p. NpM3C.2.
- [145] Z. Fang, S. Thongrattanasiri, A. Schlather, Z. Liu, L. Ma, Y. Wang, P. M. Ajayan, P. Nordlander, N. J. Halas, and F. J. García de Abajo, “Gated tunability and hybridization of localized plasmons in nanostructured graphene,” *ACS Nano*, vol. 7, no. 3, pp. 2388–2395, Mar. 2013.
- [146] N. K. Emani, T.-F. Chung, A. V. Kildishev, V. M. Shalaev, Y. P. Chen, and A. Boltasseva, “Electrical modulation of fano resonance in plasmonic nanostructures using graphene,” *Nano Lett.*, vol. 14, no. 1, pp. 78–82, 2013.
- [147] D. Rodrigo, O. Limaj, D. Janner, D. Etezadi, F. J. García de Abajo, V. Pruneri, H. Altug, F. J. Garcia de Abajo, V. Pruneri, and H. Altug, “Mid-infrared plasmonic biosensing with graphene,” *Science*, vol. 349, no. 6244, pp. 165–168, Jul. 2015.

- [148] T. J. Echtermeyer, L. Britnell, P. K. Jasnós, A. Lombardo, R. V Gorbachev, A. N. Grigorenko, A. K. Geim, A. C. Ferrari, and K. S. Novoselov, “Strong plasmonic enhancement of photovoltage in graphene,” *Nat. Commun.*, vol. 2, p. 458, Jan. 2011.
- [149] Y. Yao, R. Shankar, P. Rauter, Y. Song, J. Kong, M. Lončar, F. Capasso, M. Loncar, F. Capasso, M. Lončar, and F. Capasso, “High-Responsivity Mid-Infrared Graphene Detectors with Antenna-Enhanced Photocurrent Generation and Collection,” *Nano Lett.*, vol. 14, no. 7, pp. 3749–3754, Jul. 2014.
- [150] Y. Liu, R. Cheng, L. Liao, H. Zhou, J. Bai, G. Liu, L. Liu, Y. Huang, and X. Duan, “Plasmon resonance enhanced multicolour photodetection by graphene,” *Nat. Commun.*, vol. 2, p. 579, 2011.
- [151] T. J. Echtermeyer, S. Milana, U. Sassi, A. Eiden, M. Wu, E. Lidorikis, and A. C. Ferrari, “Surface Plasmon Polariton Graphene Photodetectors,” *Nano Lett.*, vol. 16, no. 1, pp. 8–20, 2016.
- [152] M. S. Jang, V. W. Brar, M. C. Sherrott, J. J. Lopez, L. Kim, S. Kim, M. Choi, and H. a. Atwater, “Tunable large resonant absorption in a midinfrared graphene Salisbury screen,” *Phys. Rev. B*, vol. 90, p. 165409, 2014.
- [153] S. Kim, M. S. Jang, V. W. Brar, Y. Tolstova, K. W. Mauser, and H. A. Atwater, “Electronically tunable extraordinary optical transmission in graphene plasmonic ribbons coupled to subwavelength metallic slit arrays,” *Nat. Commun.*, vol. 7, p. 12323, 2016.
- [154] A. Woessner, M. B. Lundberg, Y. Gao, A. Principi, P. Alonso-González, M. Carrega, K. Watanabe, T. Taniguchi, G. Vignale, M. Polini, J. Hone, R. Hillenbrand, and F. H. L. Koppens, “Highly confined low-loss plasmons in graphene–boron nitride heterostructures,” *Nat. Mater.*, vol. 14, no. 4, pp. 421–425, Apr. 2015.
- [155] H. Jiang, S. Choudhury, Z. Kudyshev, D. Wang, L. Prokopenko, P. Xiao, Y. Jiang, and A. Kildishev, “Enhancing sensitivity to ambient refractive index with tunable few-layer graphene/hBN nanoribbons,” *Photonics Res.*, 2019.
- [156] N. F. Mott, “Metal-insulator transition,” *Reviews of Modern Physics*, vol. 40, no. 4, pp. 677–683, 1968.

- [157] T. Driscoll, S. Palit, M. M. Qazilbash, M. Brehm, F. Keilmann, B.-G. G. Chae, S.-J. J. Yun, H.-T. T. Kim, S. Y. Cho, N. M. Jokerst, D. R. Smith, and D. N. Basov, “Dynamic tuning of an infrared hybrid-metamaterial resonance using vanadium dioxide,” *Appl. Phys. Lett.*, vol. 93, no. 2, Jul. 2008.
- [158] M. Liu, H. Y. Hwang, H. Tao, A. C. Strikwerda, K. Fan, G. R. Keiser, A. J. Sternbach, K. G. West, S. Kittiwatanakul, J. Lu, S. A. Wolf, F. G. Omenetto, X. Zhang, K. A. Nelson, and R. D. Averitt, “Terahertz-field-induced insulator-to-metal transition in vanadium dioxide metamaterial,” *Nature*, vol. 487, no. 7407, pp. 345–348, Jul. 2012.
- [159] M. D. Goldflam, M. K. Liu, B. C. Chapler, H. T. Stinson, A. J. Sternbach, A. S. McLeod, J. D. Zhang, K. Geng, M. Royal, B.-J. J. Kim, R. D. Averitt, N. M. Jokerst, D. R. Smith, H.-T. T. Kim, and D. N. Basov, “Voltage switching of a VO<sub>2</sub> memory metasurface using ionic gel,” *Appl. Phys. Lett.*, vol. 105, no. 4, p. 041117, Jul. 2014.
- [160] B. Gholipour, J. Zhang, K. F. MacDonald, D. W. Hewak, and N. I. Zheludev, “An all-optical, non-volatile, bidirectional, phase-change meta-switch,” *Adv. Mater.*, vol. 25, no. 22, pp. 3050–3054, 2013.
- [161] A.-K. U. Michel, D. N. Chigrin, T. W. W. W. Maß, K. Schönauer, M. Salinga, M. Wuttig, and T. Taubner, “Using Low-Loss Phase-Change Materials for Mid-Infrared Antenna Resonance Tuning,” *Nano Lett.*, vol. 13, no. 8, pp. 3470–3475, Aug. 2013.
- [162] A. Tittl, A.-K. U. K. U. Michel, M. Schäferling, X. Yin, B. Gholipour, L. Cui, M. Wuttig, T. Taubner, F. Neubrech, and H. Giessen, “A Switchable Mid-Infrared Plasmonic Perfect Absorber with Multispectral Thermal Imaging Capability,” *Adv. Mater.*, vol. 27, no. 31, pp. 4597–4603, Aug. 2015.
- [163] X. Yin, M. Schäferling, A.-K. U. K. U. Michel, A. Tittl, M. Wuttig, T. Taubner, and H. Giessen, “Active Chiral Plasmonics,” *Nano Lett.*, vol. 15, no. 7, pp. 4255–4260, Jul. 2015.
- [164] J. S. Chawla and D. Gall, “Epitaxial Ag(001) grown on MgO(001) and TiN(001): Twinning, surface morphology, and electron surface scattering,” *J. Appl. Phys.*, vol. 111, no. 4, p. 043708, Feb. 2012.
- [165] W. Zhao, H. Jiang, B. Liu, J. Song, Y. Jiang, C. Tang, and J. Li, “Dielectric Huygens’ Metasurface for High-Efficiency Hologram Operating in Transmission Mode,” *Sci. Rep.*, vol. 6, p. 30613, Jul. 2016.

- [166] J. Lin, P. Genevet, M. A. Kats, N. Antoniou, and F. Capasso, “Nanostructured holograms for broadband manipulation of vector beams,” *Nano Lett.*, vol. 13, no. 9, pp. 4269–4274, 2013.
- [167] M. Ozaki, J. Kato, and S. Kawata, “Surface-plasmon holography with white-light illumination,” *Science*, vol. 332, no. 6026, pp. 218–20, 2011.
- [168] M. Khorasaninejad and F. Capasso, “Broadband Multifunctional Efficient Meta-Gratings Based on Dielectric Waveguide Phase Shifters,” *Nano Lett.*, vol. 15, no. 10, pp. 6709–6715, 2015.
- [169] W. Zhao, B. Liu, H. Jiang, J. Song, Y. Pei, and Y. Jiang, “Full-color hologram using spatial multiplexing of dielectric metasurface [J],” *Opt. Lett.*, vol. 41, no. 1, p. 147, 2016.
- [170] B. Wang, F. Dong, Q.-T. Li, D. Yang, C. Sun, J. Chen, Z. Song, L. Xu, W. Chu, Y.-F. Xiao, Q. Gong, and Y. Li, “Visible-Frequency Dielectric Metasurfaces for Multiwavelength Achromatic and Highly Dispersive Holograms,” *Nano Lett.*, vol. 16, no. 8, pp. 5235–5240, Aug. 2016.
- [171] Y. Wu ... X. Li, “Intrinsic optical properties and enhanced plasmonic response of epitaxial silver,” *Adv. Mater.*, vol. 26, no. 35, pp. 6106–6110, Sep. 2014.
- [172] P. B. Johnson and R. W. Christy, “Optical constants of the noble metals,” *Phys. Rev. B*, vol. 6, no. 12, pp. 4370–4379, 1972.
- [173] E. D. Palik, “Palik, Handbook of Optical Constants, Vol.2 (AP, 1991)(ISBN 0125444222).pdf,” *Proc Natl Acad Sci USA*, vol. 2. p. Vol 2, 1991.
- [174] W. Chen, M. D. Thoreson, S. Ishii, A. V. Kildishev, and V. M. Shalaev, “Ultra-thin ultra-smooth and low-loss silver films on a germanium wetting layer,” *Opt. Express*, vol. 18, no. 5, p. 5124, Mar. 2010.
- [175] A. L. Patterson, “The Scherrer Formula for X-Ray Particle Size Determination,” *Phys. Rev.*, vol. 56, no. 10, pp. 978–982, Nov. 1939.
- [176] J. C. Ndukaife, V. M. Shalaev, and A. Boltasseva, “Plasmonics—turning loss into gain,” *Science*, vol. 351, no. 6271, 2016.
- [177] G. A. Sotiriou, F. Starsich, A. Dasargyri, M. C. Wurnig, F. Krumeich, A. Boss, J.-C. Leroux, and S. E. Pratsinis, “Photothermal Killing of Cancer Cells by the Controlled Plasmonic Coupling of Silica-Coated Au/Fe<sub>2</sub>O<sub>3</sub> Nanoaggregates,” *Adv. Funct. Mater.*, vol. 24, no. 19, pp. 2818–2827, May 2014.

- [178] H. Wang, Q. Chen, L. Wen, S. Song, X. Hu, and G. Xu, "Titanium-nitride-based integrated plasmonic absorber / emitter for solar thermophotovoltaic application," *Photonics Reseach*, vol. 3, no. 6, pp. 329–334, 2015.
- [179] N. Zhou, X. Xu, A. T. Hammack, B. C. Stipe, K. Gao, W. Scholz, and E. C. Gage, "Plasmonic near-field transducer for heat-assisted magnetic recording," *Nanophotonics*, vol. 3, no. 3, pp. 141–155, Jan. 2014.
- [180] A. Majumdar, "SCANNING THERMAL MICROSCOPY," *Annu. Rev. Mater. Sci.*, vol. 29, no. 1, pp. 505–585, Aug. 1999.
- [181] Z. J. Coppens, W. Li, D. G. Walker, and J. G. Valentine, "Probing and Controlling Photothermal Heat Generation in Plasmonic Nanostructures."
- [182] G. Baffou, P. Bon, J. Savatier, J. Polleux, M. Zhu, M. Merlin, H. Rigneault, and S. Monneret, "Thermal Imaging of Nanostructures by Quantitative Optical Phase Analysis," vol. 6, no. 3, pp. 2452–2458, 2012.
- [183] K. Maize, S. Choudhury, A. Ziabari, U. Guler, V. Shalaev, A. Kildishev, A. Boltasseva, and A. Shakouri, "Imaging of plasmonic heating in Titanium Nitride nanopillar arrays," (*Manuscript Prep.*
- [184] M. N. Libenson, "Temperature dependence of the optical constants of a metal in heating by laser radiation," *Sov. Phys. - Tech. Phys.*, vol. 13, pp. 925–31, 1969.
- [185] S. Fan, "Photovoltaics: An alternative 'Sun' for solar cells," *Nat. Nanotechnol.*, vol. 9, no. 2, pp. 92–93, Feb. 2014.
- [186] W. Shockley and H. J. Queisser, "Detailed Balance Limit of Efficiency of p-n Junction Solar Cells," *J. Appl. Phys.*, vol. 32, no. 3, pp. 510–519, Mar. 1961.
- [187] A. Lenert, D. M. Bierman, Y. Nam, W. R. Chan, I. Celanović, M. Soljačić, and E. N. Wang, "A nanophotonic solar thermophotovoltaic device," *Nat. Nanotechnol.*, vol. 9, no. 2, pp. 126–130, Jan. 2014.
- [188] O. Quevedo-Teruel ... C. Craeye, "Roadmap on metasurfaces," *J. Opt.*, vol. 21, no. 7, p. 073002, Jul. 2019.
- [189] L. Fraas and L. Minkin, "TPV History from 1990 to Present & Future Trends," in *AIP Conference Proceedings*, 2007, vol. 890, pp. 17–23.

- [190] W. R. Chan, P. Bermel, R. C. N. Pilawa-Podgurski, C. H. Marton, K. F. Jensen, J. J. Senkevich, J. D. Joannopoulos, M. Soljagic, and I. Celanovic, "Toward high-energy-density, high-efficiency, and moderate-temperature chip-scale thermophotovoltaics," *Proc. Natl. Acad. Sci.*, vol. 110, no. 14, pp. 5309–5314, Apr. 2013.
- [191] L. M. Fraas and J. Strauch, "Design and Thermal Modeling of a Portable Fuel Fired Cylindrical Tpv," in *Tpv-9*, 2010, pp. 2–7.
- [192] P. Bermel, M. Soljagic, and I. Celanovic, "Thermophotovoltaic power conversion systems: current performance and future potential," *Japanese J. Opt.*, vol. 80, no. 8, 2011.
- [193] A. Karalis and J. D. Joannopoulos, "'Squeezing' near-field thermal emission for ultra-efficient high-power thermophotovoltaic conversion," *Sci. Rep.*, vol. 6, no. 1, p. 28472, Sep. 2016.
- [194] G. Albrecht, S. Kaiser, H. Giessen, and M. Hentschel, "Refractory Plasmonics without Refractory Materials," *Nano Lett.*, vol. 17, no. 10, pp. 6402–6408, Oct. 2017.
- [195] F. Parmigiani, M. Scagliotti, G. Samoggia, and G. P. Ferraris, "Influence of the growth conditions on the optical properties of thin gold films," *Thin Solid Films*, vol. 125, no. 3–4, pp. 229–234, Mar. 1985.
- [196] C. Shemelya, D. DeMeo, N. P. Latham, X. Wu, C. Bingham, W. Padilla, and T. E. Vandervelde, "Stable high temperature metamaterial emitters for thermophotovoltaic applications," *Appl. Phys. Lett.*, vol. 104, no. 20, p. 201113, May 2014.
- [197] D. N. Woolf, E. A. Kadlec, D. Bethke, A. D. Grine, J. J. Nogan, J. G. Cederberg, D. Bruce Burckel, T. S. Luk, E. A. Shaner, and J. M. Hensley, "High-efficiency thermophotovoltaic energy conversion enabled by a metamaterial selective emitter," *Optica*, vol. 5, no. 2, p. 213, Feb. 2018.
- [198] B. Zhao, L. Wang, Y. Shuai, and Z. M. Zhang, "Thermophotovoltaic emitters based on a two-dimensional grating/thin-film nanostructure," *Int. J. Heat Mass Transf.*, vol. 67, pp. 637–645, Dec. 2013.
- [199] A. Ghanekar, L. Lin, and Y. Zheng, "Novel and efficient Mie-metamaterial thermal emitter for thermophotovoltaic systems," *Opt. Express*, vol. 24, no. 10, p. A868, May 2016.

- [200] H. Reddy, U. Guler, Z. Kudyshev, A. V Kildishev, V. M. Shalaev, and A. Boltasseva, “Temperature-Dependent Optical Properties of Plasmonic Titanium Nitride Thin Films,” *ACS Photonics*, vol. 4, no. 6, pp. 1413–1420, Jun. 2017.
- [201] J. Hu, X. Ren, A. N. Reed, T. Reese, D. Rhee, B. Howe, L. J. Lauhon, A. M. Urbas, and T. W. Odom, “Evolutionary Design and Prototyping of Single Crystalline Titanium Nitride Lattice Optics,” *ACS Photonics*, vol. 4, no. 3, pp. 606–612, Mar. 2017.
- [202] Z. J. Coppens, I. I. Kravchenko, and J. G. Valentine, “Lithography-Free Large-Area Metamaterials for Stable Thermophotovoltaic Energy Conversion,” *Adv. Opt. Mater.*, vol. 4, no. 5, pp. 671–676, May 2016.
- [203] U. Guler, A. Kildishev, V. M. Shalaev, A. Boltasseva, and G. Naik, “Refractory Plasmonic Metamaterial Absorber and Emitter for Energy Harvesting,” 2015.
- [204] Z. Kudyshev, A. Boltasseva, A. V. Kildishev, and V. M. Shalaev, “Topology optimization for refractory plasmonic applications (Conference Presentation),” in *Photonic and Phononic Properties of Engineered Nanostructures IX*, 2019, p. 54.
- [205] H. Reddy, U. Guler, A. V. Kildishev, A. Boltasseva, and V. M. Shalaev, “Temperature-dependent optical properties of gold thin films,” *Opt. Mater. Express*, vol. 6, no. 9, p. 2776, Sep. 2016.

## VITA

Sajid Choudhury graduated from Bangladesh University of Engineering and Technology (BUET), Dhaka, Bangladesh with B.Sc. and M.Sc. in Electrical and Electronic Engineering in 2009 and 2011 respectively. He served as a lecturer in BUET before coming to Purdue in Fall of 2013. Sajid worked under the guidance of Prof. Alexandra Boltasseva in Purdue towards his PhD in Electrical and Computer Engineering. Sajid worked on implementing new applications of nanophotonic devices, specific nanofabrication of metasurfaces structures. Sajid worked in the Birck Nanotechnology Center (BNC) getting experience in nanofabrication using electron beam lithography and photolithography. Sajid also gained experience in numerical modeling using finite difference time domain (FDTD) and finite element method packages. Sajid is a member of Optical Society of America (OSA), SPIE, and IEEE. Sajid served as Treasurer of OSA, representing Purdue in the Frontiers in Optics (FiO) conference 2017. Sajid served as the president of the student body of BNC, Nanotechnology Student Advisory Council (NSAC).

## PUBLICATIONS

### Journal Publications

[8] Maowen Song, Di Wang, Samuel Peana, Sajid Choudhury, Piotr Nyga, Zhaxylyk A. Kudyshev, Honglin Yu, Alexandra Boltasseva, Vladimir M. Shalaev and Alexander V. Kildishev, "Colors with Plasmonic Nanostructures: A Full-Spectrum Review" accepted for publication in Applied Physics Review (2019)

[7] Sajid Choudhury, Zhaxylyk A Kudyshev, Soham Saha, Harsha Reddy, Alexandra Boltasseva, Vladimir M Shalaev and Alexander V Kildishev, "Refractory Plasmonic Metasurfaces" a section in "Roadmap on metasurfaces", Journal of Optics 21(7) (2019)

[6] Huan Jiang, Sajid Choudhury, Zhaxylyk A Kudyshev, Di Wang, Peng Xiao, Yongyuan Jiang, Alexander V Kildishev, "Enhancing sensitivity to ambient refractive index with tunable few-layer graphene/hBN nanoribbons" Photonics Research 7(7), 815-822 (2019)

[5] Huan Jiang, Harsha Reddy, Deesha Shah, Zhaxylyk A Kudyshev, Sajid Choudhury, Di Wang, Yongyuan Jiang, Alexander V Kildishev, "Modulating Phase by Metasurfaces with Gated Ultra-thin TiN Films", Nanoscale 11, 11167-11172 (2019)

[4] Sajid M Choudhury, Di Wang, Krishnakali Chaudhuri, Clayton DeVault, Alexander V Kildishev, Alexandra Boltasseva, Vladimir M Shalaev, "Material platforms for optical metasurfaces", Nanophotonics 7 (6), 959-987 (2018)

[3] Vladimir A. Zenin, Sajid Choudhury, Soham Saha, Vladimir M. Shalaev, Alexandra Boltasseva, and Sergey I. Bozhevolnyi, "Hybrid plasmonic waveguides formed by metal coating of dielectric ridges", Optics Express Vol. 25, Issue 11, pp. 12295-12302 (2017)

[2] Sajid Choudhury, Urcan Guler, Amr Shaltout, Vladimir M. Shalaev, Alexander V. Kildishev, Alexandra Boltasseva, "Pancharatnam–Berry Phase Manipulating Metasurface for Visible Color Hologram Based on Low Loss Silver Thin Film", *Advanced Optical Materials* 2017, 5, 1700196.

[1] Jongbum Kim, Sajid Choudhury, Clayton DeVault, Yang Zhao, Alexander V Kildishev, Vladimir M Shalaev, Andrea Alù, Alexandra Boltasseva, "Controlling the Polarization State of Light with Plasmonic Metal Oxide Metasurface", *ACS Nano* vol 10, issue 10, 9326-9333 2016

### **Patents**

[1] Amr Shaltout, Sajid Choudhury, Alexander V. Kildishev, Alexandra Boltasseva, Vladimir Shalaev, "System for producing ultra-thin color phase hologram with metasurfaces", US Patent number 20160334758, filed May 11, 2016